

Multichannel experimental and theoretical constraints for the $^{116}\text{Cd}(^{20}\text{Ne}, ^{20}\text{F})^{116}\text{In}$ charge exchange reaction at 306 MeV

S. Burrello^{1,2}, S. Calabrese^{3,4}, F. Cappuzzello^{3,4}, D. Carbone³, M. Cavallaro³, M. Colonna³, J. A. Lay^{2,5}, H. Lenske⁶, C. Agodi³, J. L. Ferreira⁷, S. Firat⁸, A. Hacısalihoglu⁹, L. La Faiu^{3,4}, A. Spatafora^{3,4}, L. Acosta^{10,11}, J. I. Bellone³, T. Borello-Lewin¹², I. Boztosun⁸, G. A. Brischetto^{3,4}, D. Calvo¹³, E. R. Chávez-Lomelí¹⁰, I. Ciraldo^{3,4}, M. Cutuli^{3,4}, F. Delaunay^{3,4,14}, P. Finocchiaro³, M. Fisichella³, A. Foti¹¹, F. Iazzi^{13,15}, G. Lanzalone^{3,16}, R. Linares⁷, J. Lubian⁷, M. Morales¹⁷, J. R. B. Oliveira¹², A. Pakou¹⁸, L. Pandola³, H. Petrascu¹⁹, F. Pinna^{13,15}, G. Russo¹¹, O. Sgouros³, S. O. Solakci⁸, V. Soukeras³, G. Souliotis²⁰, D. Torresi³, S. Tudisco³, A. Yildirin⁸ and V. A. B. Zagatto⁷

(NUMEN Collaboration)

¹*Technische Universität Darmstadt, Fachbereich Physik, Institut für Kernphysik, Darmstadt, Germany*

²*Departamento de Física Atomica, Molecular y Nuclear, Facultad de Física, Universidad de Sevilla, Sevilla, Spain*

³*Istituto Nazionale di Fisica Nucleare, Laboratori Nazionali del Sud, Catania, Italy*

⁴*Dipartimento di Fisica e Astronomia “Ettore Majorana,” Università di Catania, Catania, Italy*

⁵*Instituto Carlos I de Física Teórica y Computacional, Universidad de Sevilla, Sevilla, Spain*

⁶*Institut für Theoretische Physik, Justus-Liebig-Universität Giessen, Giessen, Germany*

⁷*Instituto de Física, Universidade Federal Fluminense, Niterói, Brazil*

⁸*Department of Physics, Akdeniz University, Antalya, Turkey*

⁹*Institute of Natural Sciences, Karadeniz Teknik Üniversitesi, Trabzon, Turkey*

¹⁰*Instituto de Física, Universidad Nacional Autónoma de México, Mexico City, Mexico*

¹¹*INFN, Sezione di Catania, Catania, Italy*

¹²*Instituto de Física, Universidade de São Paulo, São Paulo, Brazil*

¹³*INFN, Sezione di Torino, Torino, Italy*

¹⁴*LPC Caen, Normandie Université, ENSICAEN, UNICAEN, CNRS/IN2P3, Caen, France*

¹⁵*DISAT, Politecnico di Torino, Torino, Italy*

¹⁶*Facoltà di Ingegneria e Architettura, Università di Enna “Kore,” Enna, Italy*

¹⁷*Instituto de Pesquisas Energeticas e Nucleares IPEN/CNEN, São Paulo, Brazil*

¹⁸*Department of Physics, University of Ioannina and Hellenic Institute of Nuclear Physics, Ioannina, Greece*

¹⁹*IFIN-HH, Bucharest, Romania*

²⁰*Department of Chemistry, University of Athens and Hellenic Institute of Nuclear Physics, Athens, Greece*



(Received 17 July 2021; revised 27 January 2022; accepted 11 February 2022; published 24 February 2022)

Background: Charge-exchange (CE) reactions offer a major opportunity to excite nuclear isovector modes, providing important clues about the nuclear interaction in the medium. Moreover, double charge-exchange reactions are proving to be a tempting tool to access nuclear transition matrix elements (NMEs) related to double beta-decay processes. The latter are also of crucial importance to extract neutrino properties from the half-life of the hypothetical neutrinoless double beta decay and to search for physics beyond the standard model.

Purpose: Through a multichannel experimental analysis and a consistent theoretical approach of the $^{116}\text{Cd}(^{20}\text{Ne}, ^{20}\text{F})^{116}\text{In}$ single charge-exchange (SCE) reaction at 306 MeV, we aim at disentangling from the experimental cross section the contribution of the competing mechanisms associated with second- or higher-order sequential transfer and/or inelastic processes.

Methods: We measured excitation energy spectra and absolute cross sections for elastic + inelastic, one-proton transfer and SCE channels by using the MAGNEX large acceptance magnetic spectrometer to detect the ejectiles. For the first two channels, we also extracted the experimental cross-section angular distributions. The experimental data are compared with theoretical predictions obtained by performing two-step distorted-wave Born approximation and coupled reaction channel calculations. We employ spectroscopic amplitudes for single-particle transitions derived within a large-scale shell-model approach and different optical potentials for modeling the initial- and the final-state interactions.

Results: The present study significantly mitigates the possible model dependence existing in the description of these complex reaction mechanisms thanks to the satisfactory reproduction of several channels at once. In particular, our work demonstrates that the two-step transfer mechanisms produce a non-negligible contribution to the total cross section of the $^{116}\text{Cd}(^{20}\text{Ne}, ^{20}\text{F})^{116}\text{In}$ reaction channel, although a relevant fraction is still missing, being ascribable to the direct SCE mechanism, which is not addressed here.

Conclusions: Our analysis provides a careful estimation of the sequential transfer processes which are competing with the direct SCE mechanism for the heavy ion reaction under investigation. The study suggests that the direct SCE should play an important role among the mechanisms populating the final channel. Nevertheless, the analysis of the higher-order processes considered here is mandatory to isolate the direct SCE process contribution and approach structure information on the corresponding NME from the reaction cross section. The description of the latter process and the competition between the two mechanisms deserves further investigation.

DOI: [10.1103/PhysRevC.105.024616](https://doi.org/10.1103/PhysRevC.105.024616)

I. INTRODUCTION

Charge-exchange (CE) transitions induced by the nuclear interaction have raised a widespread theoretical and experimental interest over the last decades, being regarded as a major source of information on nuclear isovector excitations [1–3]. On the other hand, CE reactions offer a quite appealing opportunity to excite these modes [4–11], providing crucial clues about the nucleon-nucleon (NN) interaction in the medium whose behavior in the spin-isospin channels is still not fully understood. Indeed, CE reactions are nowadays the object of intensive experimental campaigns [12–18].

In the case of high-energy reactions with light projectiles, where the reaction mechanism is rather well known, single CE (SCE) reactions have been widely investigated to probe spin-isospin properties of nuclei. Moreover, β decay was used as calibration whenever possible in view of the close relationship between β -decay strengths and CE cross sections at low momentum transfer [19,20].

A renewed interest has also recently emerged in studying CE reactions with heavy ions, which are used to address a wide spectrum of research topics, from work on quasi-elastic SCE excitations with low- and intermediate-energy ion beams, to investigations of the subnuclear sector by excitations of nucleon resonance, e.g., $\Delta_{33}(1232)$, at relativistic beam energies, as discussed in the recent review article [21].

Over the years, a plethora of heavy ion SCE data has been collected and used for spectroscopic work. The study of the charge-converting components of the projectile-target nucleon-nucleon (NN) interactions has been in many cases the driving force behind experimental and theoretical research. In this context, some progress on the theoretical description of the complex reaction dynamics has been made over the past years [21–23]. Not in the least, the interest in that kind of interaction is motivated by the similarity of the nuclear transition operators to those acting in nuclear beta decay, as elucidated in Refs. [21,22,24,25].

Even the large research potential of heavy ion double charge-exchange (DCE) reactions was recognized quite early in a first (unsuccessful) attempt to study the double Gamow–Teller (DGT) mode [6]. More recently, experimental studies have also been investigating the DCE reactions between heavy ions to identify the connections of these processes not only with DGT or double Fermi transitions but also with double- β (2β) decay [24,26]. In this context, the NUMEN and NURE projects at LNS-INFN have proposed an innovative way to exploit DCE reactions to access nuclear transition matrix elements (NME) related to those involved in 2β decay [12]. A very accurate knowledge of the NME is indeed

instrumental to extract the properties of neutrinos from the half-life of the hypothetical neutrinoless double beta decay ($0\nu 2\beta$), that is, to search for physics beyond the standard model [27,28]. Besides, extraction of nuclear structure information from the total DCE reaction cross section is helpful to add new and more stringent constraints on the nuclear models [27,29]. These goals pose an exciting challenge on the study of DCE reactions that are stimulating recent developments, aimed to describe the (virtually unexplored) underlying reaction mechanism [24,26]. Before being able to address those spectroscopic issues on a quantitative level, the experimental and theoretical research program of the NUMEN and NURE projects demands thus a full understanding of the reaction mechanism of the underlying SCE and DCE reactions at beam energies in the region of 10 to 20 A MeV, which is located well above the Coulomb barrier in practical experiments.

Heavy ion collisions above the Coulomb barrier are, however, generally characterized by a large number of different populated channels. For example, it is well known that nuclear charge-exchange processes proceed in principle by two distinct but interfering mechanisms. Direct CE is a collisional process mediated by isovector nucleon-nucleon (NN) interactions acting between projectile and target. However, an unwanted but unavoidable complication in the heavy-ion-induced CE reactions is the admixture of multistep reaction mechanisms, typically given by sequential transfer of nucleons or inelastic processes of second or higher order [30]. The two-step transfer mechanism is indeed sensitive to the nucleon-nucleus mean-field potential and cannot probe the NN interaction responsible for Fermi and Gamow–Teller isospin-flip transitions, which are observed in a CE reaction [31]. For SCE reactions, the competition of one-step direct charge exchange and two-step sequential processes was discussed in detail, e.g., in Refs. [4,32–34]. Fully microscopic theoretical investigations of heavy ion SCE reaction showed that, at energies close to the Coulomb barrier, transfer CE is by far the dominant reaction mechanism [4] but, with increasing beam energy, the strength of direct SCE rapidly increases and finally dominates the SCE cross sections [34].

In Ref. [34] it was also shown that direct CE calculations give differential cross-section angular distributions with a steeper decrease at backward angles than the experimental data, so indicating the increased importance of higher-order processes at large momentum transfer. Other pioneering studies [35] showed that, under suitable conditions, the sequential transfer of proton and neutron pairs could even constitute the dominant process populating the final channel of a DCE reaction, at least when not-very-forward angles were considered.

The second-order character and the dominance of the mean-field dynamics lead to a quite pronounced dependence of transfer SCE on incident energies, quantum numbers, and matching conditions of the involved single-particle orbitals, and the structure and multipolarities of the initial, intermediate, and final states, see, e.g., Ref. [34]. In other words, although the reaction mechanism follows general rules, the transfer SCE yield may depend critically on the reacting nuclei and the kinematical conditions and a full understanding of the competition between the different mechanisms calls for further investigation. To complicate matters, one should take into account that projectile and target inelastic excitations could also play a relevant role in the description of the reaction mechanism, producing strong coupling effects among the various reaction channels. Therefore, if one wants to extract information on the NME, it is mandatory to disentangle from the experimental CE cross section the contribution of each competing process.

On the other hand, the theoretical description of the complex mechanisms involved requires several ingredients whose reliability cannot be generally guaranteed when applied beyond the domain in which they have been determined. For instance, the nucleus-nucleus potential should be in principle specifically modeled for the projectile-target system under investigation. However, recent studies have shown that, in the energy region of our interest, a satisfactory reproduction of the scattering cross sections is achieved for a wide range of masses under suitable general prescriptions [23,36–39]. It is nonetheless important to validate this strategy for each system under investigation and, in this context, the experimental measurement and analysis of the elastic and inelastic scattering is thus crucial to constrain the SCE and DCE calculations.

Because of the complexity in diagonalizing the Hamiltonian of systems involving open-shell medium and heavy nuclei, other requirements are then also needed to perform the nuclear structure calculations. In particular, further constraints are required for the model space and interaction combination which is frequently adopted to deduce the single-particle transitions characterizing one- and two-nucleon transfer processes [38,40,41]. A comprehensive analysis should take the limitations of the model spaces into account and assess whether the global interaction parameters are suitably applicable to the system under investigation.

A possible gateway to overcome this issue, which has proven successful in some recent works [23,38], is to try to perform measurements of several reaction mechanisms under the same experimental conditions and to describe them within a unified theoretical reaction scheme. In the present work, we propose thus to perform a multichannel experimental analysis to be compared with a combined structure and reaction theoretical study, with the aim to assess the reliability of the ingredients adopted in the description of the involved mechanisms.

As part of the intensive experimental campaigns proposed by the NUMEN project, we focus on the $^{116}\text{Cd}(^{20}\text{Ne}, ^{20}\text{F})^{116}\text{In}$ SCE reaction at 306 MeV. ^{116}Cd was chosen as a target not in the least because that nucleus is one of the candidates for the pursued $0\nu 2\beta$ decay [16]. Keeping that goal in mind, there are other, lighter nuclei under

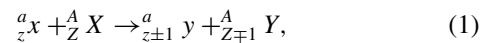
scrutiny as 2β -decay candidates. However, once reactions on ^{116}Cd are understood, then SCE—and finally DCE—reactions on lighter target nuclei can be analyzed accordingly by the same methods.

The goal of this paper is twofold: first of all, the work serves to show the experimental feasibility of such a demanding reaction for spectroscopic purposes. Second, on the theory side we aim at the evaluation of the various competing transfer contributions feeding the outgoing SCE channel by a comparison with a more comprehensive set of experimental observables beyond what has been done so far.

The paper is organized as follows: In Sec. II we illustrate the theoretical framework adopted, trying to underline the main differences existing among the various reaction schemes considered. In Sec. III the experimental setup and the data reduction are described. In Sec. IV we discuss the results concerning the analysis of the elastic scattering, the one-proton transfer reaction, and the sequential-nucleon transfer processes. In the last section, conclusions are drawn and future perspectives are indicated.

II. THEORETICAL FRAMEWORK

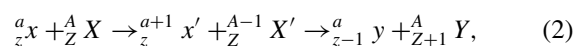
We consider an ion-ion SCE reaction according to the scheme



leading from the entrance channel $\alpha = \{x; X\}$ to the exit channel $\beta = \{y; Y\}$. In the outgoing nuclei, states of multipolarity J^π are excited, including Gamow–Teller modes of unnatural parity $\pi = (-)^{J+1}$ and Fermi modes of natural parity, $\pi = (-)^J$, respectively. During the reaction, the mass partition is retained but the charge partition is changed, either by a balanced redistribution of protons and neutrons in a sequence of single-particle transfer reactions or by direct single charge exchange.

Direct SCE is mediated by the exchange of (virtual) isovector mesons between nucleons in projectile and target. It is a process of first order in the projectile-target isovector interaction, described well by distorted-wave Born approximation (DWBA) methods. Hence, in direct SCE the initial and final states are connected in an especially simple manner by transition operators of the same spin-isospin structure as known from nuclear beta decay [21,22]. From the point of view of nuclear structure physics, the direct SCE reaction mechanism is the by far preferred mechanism because of the unfiltered access to nuclear isovector spectroscopy.

However, the same exit channels may also be populated in a considerably more complicated manner by transfer SCE. That alternative process requires a sequence of proton-neutron exchange processes between projectile and target nuclei, finally merging into a configuration which is part of the wave function of the final state. Obviously, that process requires the appropriate stepwise rearrangement of neutrons and protons. In a reaction like the one here investigated, we encounter the neutron-pickup proton-stripping sequence



and the complementary proton-stripping neutron-pickup sequence

$${}^a_x + {}^A_Z X \rightarrow {}^{a-1}_{z-1} y' + {}^{A+1}_{Z+1} Y' \rightarrow {}^a_{z-1} y + {}^A_{Z+1} Y, \quad (3)$$

both being at least second-order reactions in the respective mean-field potentials defining the transfer interactions. From a nuclear structure point of view, transfer SCE is probing the overlap of the final projectile and target configurations with specific proton and neutron configurations. Since these configurations are populated stepwise in a sequence of pickup and stripping reactions, the single-particle spectroscopy in the intermediately reached $A \pm 1$ and $a \mp 1$ nuclei, respectively, also plays an important role. Moreover, in order to exhaust the full single-particle strengths, the transfer steps should in principle scan over the whole spectral distributions for each single-particle spin and parity.

Also admixtures of core-excited configurations may affect significantly the spectroscopic distributions, especially in the intermediately populated odd-even and even-odd nuclei. A complete theoretical analysis might require also taking into account the coupling of the various channels to inelastically excited states in projectile- and target-like nuclei. The proper handling of these complexities in the reaction mechanism requires methods going beyond the standard DWBA.

At this stage we do not consider direct SCE processes further, mainly due to yet to be resolved conceptual uncertainties with respect to the consistency of the theoretical models. The widely used standard approach to the nuclear response function of direct SCE is the quasiparticle random-phase approximation (QRPA). The QRPA by definition focuses on the nuclear one-particle–one-hole response in a quite complete manner, even over very large energy intervals as entering, e.g., as intermediate states into the theory of DCE reactions [24,25]. The spectroscopy of the transfer channels, however, is described by many-body shell-model methods, which emphasize the multiconfiguration dynamics in a limited number of the nuclear valence shells. Thus, in order to exclude arbitrary effects due to possibly incommensurable theoretical input, at this point we refrain from combining the two distinct sectors, leaving that demanding task to later work.

It is worthwhile to notice that the strong absorption in the overlap region enforces the localization of the interaction regions mostly to the surface or even tail regions of the density distributions of the colliding ions. Different direct reaction frameworks are available to tackle such processes. First, the DWBA framework has proven in many cases to describe successfully direct reactions as single nucleon transfer reactions [38,42–45]. For a reaction $\alpha \rightarrow \beta$ the DWBA amplitude is given as a matrix element of distorted waves $\chi_{\alpha\beta}^{(\pm)}$ and a form factor or reaction kernel

$$M_{\alpha\beta} = \langle \chi_{\beta}^{(-)} | F_{\alpha\beta} | \chi_{\alpha}^{(+)} \rangle, \quad (4)$$

where the nuclear structure information is contained in the (nonlocal) reaction kernel

$$F_{\alpha\beta}(\mathbf{r}_{\alpha}, \mathbf{r}_{\beta}) = \langle yY | U_{\alpha\beta} | xX \rangle, \quad (5)$$

depending on the channel coordinates \mathbf{r}_{α} and \mathbf{r}_{β} . The transition potential $U_{\alpha\beta}$ accounts for the nuclear dynamics of the reaction. For single nucleon transfer reactions, $U_{\alpha\beta}$ is defined

in terms of the binding potentials of the transferred nucleon plus eventually necessary nonorthogonality terms; for details, see, e.g., Refs. [42,46]. In the case of a second-order reaction like transfer SCE, $U_{\alpha\beta}$ is by itself a second-order operator, accounting for the population of the intermediate states and the corresponding distorted-wave channel propagators, see Refs. [24,25].

A widely used successful approach is to separate the transition potentials into (products of) spectroscopic amplitudes determined either by nuclear theory or phenomenologically by fits to data, and reduced form factors carrying the information on single-particle wave functions and potentials. The calculations discussed below are performed with realistic single-particle wave functions and potentials describing separation energies and nuclear radii. Spectroscopic amplitudes are taken from many-body shell-model calculations.

The DWBA approximation assumes, however, that the probability of the process under study is small with respect to the elastic scattering and requires that the final state is reached directly, i.e., without any intermediate excitations of excited states lying in the same mass partitions. Such a requirement is not always fulfilled, especially in the case of strongly excited rotational or vibrational modes. As a result, when coupling effects among the various reaction channels are strong, the DWBA approach fails to reproduce the experimental data. For such cases, the reaction should be described by solving a set of coupled wave equations. For the direct solution of such coupled channels (CC) problems, standard numerical methods are available, but restricted to couplings within the same mass partition. Iterative methods are used if transfer channels are to be included. A widely used approach is the coupled channels Born approximation (CCBA). On top of the CCBA solutions, the coupling of initial and final SCE channels via sequential transfer is added iteratively by the coupled reaction channel (CRC) formalism. For details we refer again to the literature [42,46,47]. The various formal approaches are realized numerically in the exact finite-range (EFR) computer code FRESKO [48], which treats properly the aforementioned nonlocalities of transfer form factors. FRESKO was used for all reaction calculations.

In the following sections, we first study elastic scattering. As discussed in Ref. [21], the order of magnitude of the quasi-elastic CE and transfer cross sections is determined by the distorted waves. Their properties are fixed by the optical potentials used to describe elastic scattering. Hence, a proper description of elastic cross sections and total reaction cross sections is essential for a realistic transfer yield. Therefore, below some space is devoted to elastic scattering and the derivation of optical potentials. Turning to the transfer SCE, we start by studying the population of several low-lying excited states reached in the first step of the full SCE sequence. All of them are relevant intermediate channels of the nucleon transfer processes which coherently contribute to the full SCE reaction. Finally, the transitions to the final SCE states are considered by investigating the combined sequential one-neutron–one-proton transfer rearrangements. Further details concerning each reaction framework, the description of the ion-ion interaction, as well as the structure ingredients

required within our scheme will be provided especially in Sec. IV.

III. EXPERIMENT AND DATA REDUCTION

The experiment was performed at the INFN-LNS laboratory in Catania. A $^{20}\text{Ne}^{4+}$ beam was accelerated at 306 MeV incident energy by the K800 Superconducting Cyclotron, fully stripped by crossing a thin carbon foil located at the accelerator exit and then transported to the scattering chamber. The targets were 96% isotopically enriched ^{116}Cd foils produced by rolling at the LNS target laboratory of thickness (1370 ± 70) , (1080 ± 60) , and (1330 ± 70) $\mu\text{g}/\text{cm}^2$ in the case of one-proton transfer, SCE, and scattering measurements, respectively. The first two were coupled to natural C foils with thicknesses of (990 ± 50) and (900 ± 45) $\mu\text{g}/\text{cm}^2$, while the third one was coupled to a CH_2 foil (950 ± 45) $\mu\text{g}/\text{cm}^2$ thick. Such poststripper foils were introduced [49,50] to conveniently readjust the charge state distribution of the ions emerging from the cadmium targets [51]. However, due to the kinematics of the explored reactions, the data shown in the following are not affected, in the analyzed regions, by the contributions due to reactions on poststripper materials. A copper Faraday cup of 0.8 cm entrance diameter and 3 cm depth was used in order to stop the beam and collect its charge. It was mounted 15 cm downstream of the target and equipped with an electron suppressor polarized at -200 V to ensure, even with beam currents of few *enA* as those typically available in the described experimental conditions [12], a charge collection accuracy better than 10%. The reaction ejectiles were momentum analyzed by the MAGNEX spectrometer [52], whose experimental setup was optimized to select, in separate runs, specific reaction channels:

- (i) For the $^{116}\text{Cd}(^{20}\text{Ne}, ^{20}\text{Ne})^{116}\text{Cd}$ elastic- and inelastic-scattering measurement, the spectrometer optical axis was set at three different angular settings, $\theta_{\text{opt}} = 8^\circ$, 13° , and 20° in the laboratory frame, spanning the $3^\circ < \theta_{\text{lab}} < 26^\circ$ angular range. All the runs were performed by adopting the full angular acceptance ($\Omega \approx 50$ msr).
- (ii) For the $^{116}\text{Cd}(^{20}\text{Ne}, ^{19}\text{F})^{117}\text{In}$ one-proton transfer measurement the spectrometer optical axis was placed at $\theta_{\text{opt}} = 8^\circ$, corresponding to the $3^\circ < \theta_{\text{lab}} < 14^\circ$ angular range. The MAGNEX angular acceptance was slightly decreased, determining a solid angle of ≈ 45 msr.
- (iii) For the $^{116}\text{Cd}(^{20}\text{Ne}, ^{20}\text{F})^{116}\text{In}$ single charge exchange, the spectrometer optical axis was oriented at $\theta_{\text{opt}} = 9^\circ$, thus exploring the angular range $4^\circ < \theta_{\text{lab}} < 15^\circ$. In this run the vertical angular acceptance was considerably reduced in order to limit the overall event rate at the focal plane detector, decreasing the covered solid angle to ≈ 1.3 msr.

The ejectile identification as well as the data reduction techniques are described in detail in Refs. [49,53]. They require the accurate measurements of the horizontal and vertical positions and angles provided by the MAGNEX focal plane

detector [54,55] and knowledge of the high-order transport map of the particles throughout the spectrometer [52].

The differential cross sections were extracted for all the measured reaction channels according to the technique described in Ref. [52]. The error bars reported in the corresponding energy and angular distributions account for the statistical contribution, the uncertainty due to the solid angle evaluation and the fit procedure when performed. A systematic uncertainty of $\approx 10\%$, not shown in the plots, is common to all the experimental data, originating from target thickness measurement and Faraday cup charge collection uncertainties.

IV. RESULTS

A. Scattering channel

A crucial issue for a quantitative understanding of heavy ion reactions is the proper treatment of the projectile-target interaction, thus motivating elastic- and inelastic-scattering studies.

The excitation energy spectrum of the ($^{20}\text{Ne}, ^{20}\text{Ne}$) scattering channel is shown in Fig. 1, being $E_x = Q_0 - Q$ with Q_0 being the ground-state to ground-state Q value. The limited experimental energy resolution ($\delta E \approx 1.1$ MeV full width half maximum, mainly due to straggling effects in the used target) and the available statistics do not allow us to discriminate the elastic transition and the first-excited state of the system, the (2_1^+) state of the ^{116}Cd expected at 0.513 MeV, except for a restricted angular region ($15^\circ \lesssim \theta_{\text{lab}} \lesssim 18^\circ$). In Fig. 1(a), the sum of the contributions of such states is represented by the dominant Gaussian function, whereas in Fig. 1(b) the two transitions are considered separately. Additional Gaussian functions peaked around 1.24 and 1.64 MeV, introduced to better reproduce the bump visible in such an energy region, are shown in Figs. 1(a) and 1(b). These distributions are expected to correspond to the sum of the cadmium two-phonon quadrupole states (2^+ , 4^+ , 0^+) at 1.213, 1.219, 1.282 MeV, respectively, and the (2^+) ^{20}Ne and ^{116}Cd states at 1.634 and 1.642 MeV, respectively. However, they can also collect the contributions from other possible states such as the ^{116}Cd (0^+) state predicted at 1.382 MeV and, partially, from the cadmium states foreseen around 2 MeV. The excitation energy spectrum of Fig. 1(b), corresponding to the backward angular range, presents a further Gaussian distribution introduced to better model the counting shape observed around 2.2 MeV, which is attributable to the latest quoted excited states of the target as well as to the simultaneous excitation of the first target and projectile transitions. Due to the low yields, the high number of the involved possible states and the limited energy resolution available which does not allow us to distinguish between the different possible transitions, the distributions lying beyond 1 MeV will not be further considered in the following. Finally, the experimental spectrum beyond the commented structures resulting in a continuous and suppressed shape is fit by a smooth curve. The experimental differential cross section of the quasi-elastic transition, which includes the ground state (g.s.) and the (2_1^+) state of ^{116}Cd at 0.513 MeV, is shown in Fig. 2(a) and compared with the results of the theoretical calculations. The experimental

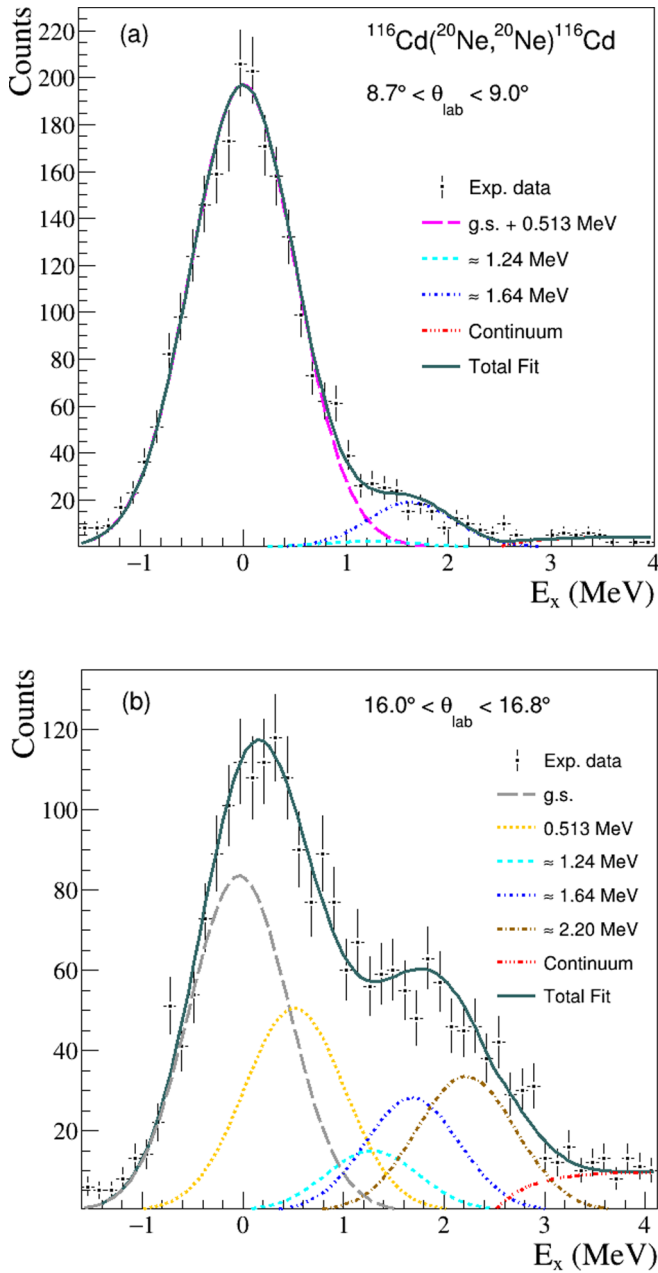


FIG. 1. Excitation energy spectra of the scattering channel in two different angular regions. (a) Energy spectrum in the angular range $8.7^\circ < \theta_{\text{lab}} < 9.0^\circ$. The magenta curve represents the energetically unresolved ground and first-excited states of the target. The cyan and blue Gaussian functions are introduced to reproduce the small bump associated with the unresolved excitation of the first low-lying states of ^{116}Cd and ^{20}Ne (see text). The red curve reproduces the continuous spectrum in the excitation energy region above ≈ 2.5 MeV. The sum of all the mentioned contributions is shown as the green line. (b) Energy spectrum in the angular range $16.0^\circ < \theta_{\text{lab}} < 16.8^\circ$. The ground and the first ^{116}Cd excited states are fit separately as the gray and yellow curves. The brown curve represents the additional Gaussian functions peaked around 2.2 MeV and that are not present in the forward angle spectrum of panel (a). For all the other contributions as well as for the total sum function, the same color code as in panel (a) is adopted.

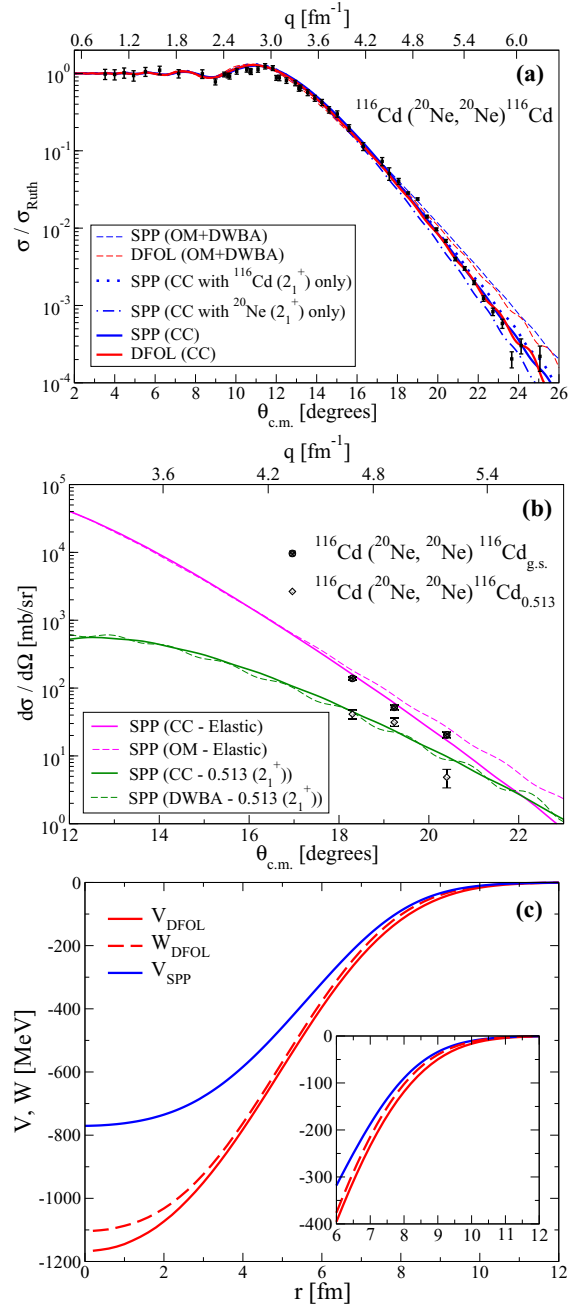


FIG. 2. (a) Experimental angular distribution of differential quasi-elastic-scattering cross sections in the $\sigma/\sigma_{\text{Ruth}}$ representation. Theoretical results obtained for the DFOL (red lines) and SPP (blue lines) potentials, within two different reaction schemes, namely OM (elastic) + DWBA (inelastic), in dashed lines, and CC, in full lines. Both experimental values and theoretical calculations also include the contribution of the inelastic scattering to the (2_1^+) target state. The dotted and dashed-dotted lines show the results obtained with SPP by alternatively switching on the contributions of the (2_1^+) target and projectile states, respectively. (b) Experimental angular distribution of differential cross section for elastic and (2_1^+) ^{116}Cd inelastic excitation, as separately considered and compared with OM and DWBA or CC calculations, with the SPP potential. (c) Radial dependence of the real V (red full line) and imaginary W (red dashed line) part for DFOL and the real part V for SPP (blue full line). The inset shows also a zoom on the peripheral region.

elastic and (2_1^+) ^{116}Cd inelastic differential cross sections, as extracted in the restricted angular range indicated above, with the corresponding calculations, are reported separately in Fig. 2(b). Figures 2(a) and 2(b) also report the scale of transferred linear momentum q . As seen from the upper abscissa of Fig. 2(a), the data cover a large range of linear momentum transfers, extending from $q \approx 0.6 \text{ fm}^{-1}$ to $q \approx 6 \text{ fm}^{-1}$. Thus, heavy ion reactions of this kind are probing nuclear properties in much detail.

In the present work, the ion-ion interaction is described by a complex optical potential U , whose radial dependence is microscopically derived by doubly folding the one-body g.s. projectile and target nuclear densities, which are parametrized by two-parameter Fermi-Dirac distributions, with an effective NN interaction. In the numerical calculations of this work, two different double-folding optical potentials will be tested.

On the one hand, we consider the São Paulo potential (SPP) [56], which has already demonstrated success in describing the elastic scattering and peripheral reaction channels for several heavy-ion reactions involving light- [57,58], medium- [36,59,60], and heavy-mass [61] targets in a wide energy region.

The general SPP parametrization, being based on theoretical calculations with the Dirac-Hartree-Bogoliubov model and also on experimental results for charge distributions has no adjustable parameters [56]. However, small deviations around the average values might be expected due to the effects of the structure of the nuclei.

On the other hand, another optical potential, which was used in some other works [22,25,30] and labeled as DFOL, is employed. The latter makes use of the complex NN T -matrix derived by Franey and Love [62], including both the isoscalar and isovector components and is extrapolated down to the present energy region. Differently from the SPP case, where the imaginary part is obtained from a simple scaling of the real one, for the DFOL optical potential the imaginary potential is directly available from the folding procedure.

As briefly addressed in a recent paper [25], we are fully aware of the changes of the T -matrix to be expected in the low-energy region. Results of a recent investigation show that, below $T_{\text{lab}} = 50 \text{ MeV}$, the strength of the real parts of the (antisymmetrized) spin-scalar, isoscalar, and isovector components of the NN T -matrix remains almost constant, while the imaginary parts increase on a moderate level. A comparison of the total neutron-proton cross section to data and to the one obtained with the CD Bonn potential in the full Lippmann-Schwinger formalism shows that the strong increase of the cross section towards low energies is mainly driven by kinematical effects. The NN T -matrix parameters, as obtained for the central interactions at $T_{\text{lab}} = 15 \text{ MeV}$ in the relevant channels for the ion-ion potentials, i.e., the spin-scalar ($S = 0$) and the isospin $T = 0, 1$ channels, are given in Table I.

Although the folding procedure is easily extended to cover deformed-matter distributions of projectile and target, in the present case for numerical reasons we use spherical density profiles in the calculations of the DFOL and SPP optical potentials. In a more extended approach, reaction observables

TABLE I. Nucleon-nucleon T -matrix interaction strengths at $T_{\text{lab}} = 15 \text{ MeV}$ in the spin-scalar ($S = 0$) and the isospin $T = 0, 1$ channels. The ranges are expressed in fm, and all other quantities are in MeV.

Range	SE	TE	SO	TO
	Real			
0.25	6048.76	7972.38	-51218.10	2091.19
0.40	-1754.49	-2235.67	5541.75	-641.32
1.40	-10.50	-10.50	31.50	3.50
	Imaginary			
0.25	-1328.78	20805.12	31381.92	16175.65
0.40	-382.85	-6968.75	-4100.90	-2485.94

need to be averaged anyway over the orientations of the deformed ions. To a good approximation, the resulting net effects can be simulated by slightly changing the geometrical parameters of the density distributions [36]. In particular, since the g.s. quadrupole moment of projectile and target are not negligible [63,64], one may infer that, especially in the case of ^{20}Ne , the nucleus is significantly deformed, as also confirmed by the large experimental values of the quadrupole deformations ($\beta_2^C = 0.721$ for ^{20}Ne , $\beta_2^C = 0.194$ for ^{116}Cd). An effective way to take this aspect into account in building the optical potential is thus a change of the density profiles, as also described in Ref. [36], with the requirement to keep constant the volume integral of the nuclear densities to fix the number of nucleons. In Ref. [36], where a different reaction involving the same projectile nucleus was analyzed, an effective geometrical modification in the nuclear densities was introduced, increasing by 5% the radius of the density profiles, while renormalizing the central density parameter. For sake of consistency, the same prescription is here adopted for the projectile ^{20}Ne , while a smaller modification (3%) is used for the target to achieve the best possible agreement between data and calculations. The root mean square radius and volume integral per nucleon, as obtained for the real and the imaginary parts of both potentials adopted here, are listed in Table II. One observes that, even though the root mean square radii of the real parts practically coincide, a significant difference exists among the volume integrals of the two optical potentials, although both values are still compatible with the typical ones expected from the systematics [65].

It is worthwhile to recall that, for the imaginary part, a scaling factor has then to be introduced, depending on the reaction framework adopted, to account for missing couplings to states not explicitly considered here.

TABLE II. Real J_V and imaginary J_W part of the volume integral per nucleon (in MeV fm^3) and root mean square radii (in fm) for the real $(\langle R^2 \rangle_V)^{1/2}$ and imaginary $(\langle R^2 \rangle_W)^{1/2}$ part of DFOL and SPP potentials adopted.

	J_V	J_W	$\sqrt{\langle R^2 \rangle_V}$	$\sqrt{\langle R^2 \rangle_W}$
DFOL	-437.56	-408.94	5.884	5.770
SPP	-331.68	-331.68	5.883	5.883

Although it is not obvious that the same scaling factors should be assumed for different nuclear systems, the most reasonable choice would be to adopt a consistent approach with the analysis of some previous works [66–69]. For both DFOL and SPP optical potentials, such a factor is then set to 0.78 in the case of optical model (OM) calculations and 0.6 whenever CC calculations are performed.

A comparison with the measured quasi-elastic scattering data in terms of the corresponding Rutherford cross section σ_{Ruth} is shown in Fig. 2(a). Actually, as already explained in the previous section, the experimental values for the quasi-elastic channel include also the inelastic scattering to the (2_1^+) target state at 513 keV. Therefore, the OM (for the elastic) + DWBA (for the inelastic) calculations plotted in Fig. 2(a) take into account the incoherent sum of the two different contributions, namely, the genuine elastic cross section and the DWBA cross section of inelastic scattering to the first-excited state of ^{116}Cd .

Despite the differences existing in the internal region of the two optical potentials, there is no significant difference between the cross sections obtained by the two calculations. This fact confirms that the theoretical description of elastic scattering is not strongly dependent on the choice of these optical potentials since the strong absorption confines the reaction source on the surface of the colliding systems, where the two potentials have a similar behavior.

Heavy ion reactions and therefore elastic scattering and peripheral inelastic reactions are indeed mainly sensitive to the nuclear surface regions of the interacting nuclei and, as a result, the incoming flux is mostly absorbed into a multitude of reaction channels, as demonstrated also by the large total reaction cross sections.

One observes that theoretical OM + DWBA calculations fail to reproduce the slope exhibited by the experimental data beyond the grazing angle, whatever optical potentials are employed, including the two considered here. Since the behavior around the grazing angle is properly reproduced, the present case is similar to the one discussed in Ref. [36], where the observed discrepancies with respect to the experimental data were attributed to the coupling of the elastic channel with possible inelastic excitations to the 2_1^+ states of both projectile and target. Therefore, in Fig. 2(a), CC calculations performed with both DFOL and SPP optical potentials are also included.

Both one-step DWBA and CC calculations are performed within the rotational model, following the same prescription adopted in some recent works [23,39], despite that the low-lying states in ^{116}Cd nuclei might appear to be of a vibrational nature. Reduced transition probabilities $B(E2; 0^+ \rightarrow 2^+) = 0.0333 e^2 b^2$ for ^{20}Ne and $B(E2; 0^+ \rightarrow 2^+) = 0.58 e^2 b^2$ for ^{116}Cd are taken from Refs. [63,70,71] and used to describe the strength of Coulomb deformation of both projectile and target.

Nuclear deformations are described in terms of the first-order derivative of the OM potential $U(r)$:

$$V(r) = -\frac{\delta_2}{\sqrt{4\pi}} \frac{dU(r)}{dr}, \quad (6)$$

where the strength of the deformation is embedded in the deformation length δ_2 [42]:

$$\delta_2 = \beta_2 R = \frac{4\pi}{3Z} \frac{\sqrt{B(E2; 0^+ \rightarrow 2^+)}}{R_V}. \quad (7)$$

In Eq. (7), β_2 is the deformation parameter characterizing the transition of the given nucleus of charge Z , $R = 1.2A^{1/3}$ is the radius, and R_V is the root mean square radius of the real part of the adopted optical potential (see Table II). The deformation lengths obtained following such a prescription are $\delta_2 = 1.299$ fm and $\delta_2 = 1.130$ fm, for projectile and target, respectively. Exploratory calculations changing the method for the determination of R_V give, however, similar results. Moreover, the same radial form factors are assumed also for the imaginary coupling potentials.

One observes that the CC calculations well reproduce the slope exhibited by the quasi-elastic experimental data also at larger angles. A better agreement is thus observed with respect to OM + DWBA, especially in the region of larger momentum transfer, confirming the relevant role played by these rotational (collective) 2_1^+ states, whose couplings with the g.s. have to be explicitly included. By alternatively switching off the contributions of the various inelastic excitations, we found, moreover, a leading role played by the projectile 2_1^+ state, which is strongly coupled to the elastic channel because of its large deformation parameter. The best agreement is, however, achieved only when the combined effect with the target inelastic excitation is included.

The overall outcome is, moreover, not significantly influenced by the small changes introduced in the target and projectile nuclear density radii. Indeed, we checked that, when ignoring such modifications, the total cross section in the elastic channel differ at most by 3% with respect to the results shown before, both in the OM and in the CC approach, in the case of the SPP potential.

A further validation of the ingredients adopted in the description of the scattering channel analysis is reported in Fig. 2(b). Indeed, a nice agreement is obtained between experimental data and theoretical predictions when disentangling the elastic and the first-inelastic transitions in the angular range considered, especially when the CC calculations are performed. In Fig. 2(b), only the SPP potential is considered, although an analogous result is obtained in the case of the DFOL potential. Despite the limitedness of the angular range considered, such a result strengthens all the conclusions drawn from the quasi-elastic analysis. In particular, the matching between the experimental and theoretical elastic distribution confirms the reliability of the prescriptions adopted for the optical potentials, whereas the first inelastic transition provides another proof of the model assumed to describe the coupling with the inelastic excitations considered. In the following sections, we explicitly take into account the effect of these inelastic excitations, looking also at their influence on the transfer channels investigated within our study.

B. One-proton transfer $^{116}\text{Cd}(^{20}\text{Ne}, ^{19}\text{F})^{117}\text{In}$ reaction

The excitation energy spectrum measured for the ($^{20}\text{Ne}, ^{19}\text{F}$) one-proton transfer reaction is presented in Fig. 3.

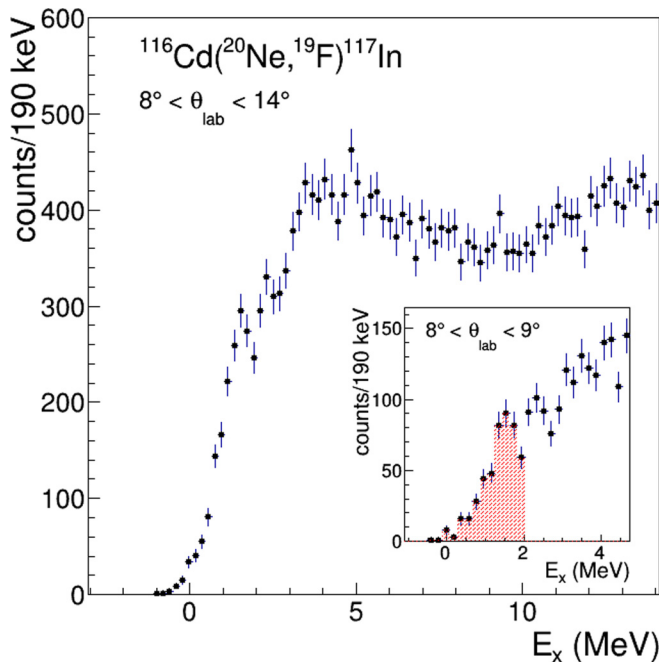


FIG. 3. Excitation energy spectrum of the one-proton transfer channel in the $8^\circ < \theta_{\text{lab}} < 14^\circ$ angular range. In the inset, the spectrum up to ≈ 4.5 MeV for the interval $8^\circ < \theta_{\text{lab}} < 9^\circ$ is reported. The red hatched area corresponds to the analyzed region, as described in the text.

In agreement with Brink's transfer matching conditions [72], the spectrum is peaked around $E_x^{\text{opt}} \approx 5$ MeV. To extract the differential cross section angular distribution in the low-excitation-energy region, the spectra have been analyzed in one-degree angular steps. The inset of Fig. 3 shows the experimental energy distribution in the $8^\circ < \theta_{\text{lab}} < 9^\circ$ interval up to ≈ 4.5 MeV. Countings at low excitation energy are smoothly distributed due to the ^{117}In and ^{19}F high nuclear level densities without exhibiting any clear structure in such a region. In fact, even if the ground-state to ground-state transition as well as the first-excited states cannot be distinguished due to the limited energy resolution, none of them dominates over the others, thus resulting in a continuous yield trend. Beyond 1 MeV, instead, some bumps are visible which are expected to be the unresolved sum of several different transitions. Examining the inset of Fig. 3, however, a local minimum is observed around 2 MeV. Then the differential cross-section angular distribution in the $[-1, 2]$ MeV excitation energy range was extracted and is shown in Fig. 4. We limited to the lowest excitation energy region, where the reproduction of the energy spectrum in terms of single-particle configurations adopted in the following calculations is expected to be more reliable. It is interesting to note that the angular distribution shape results clearly peaked close to the grazing angle ($\theta_{gr} \approx 15^\circ$) region. This “bell-shaped” behavior is the typical feature expected in absorptive reactions involving heavy nuclei [40,67,73].

Once the initial-state interaction has been properly addressed, it would be important to check whether the theoretical framework adopted in our work allows us to also

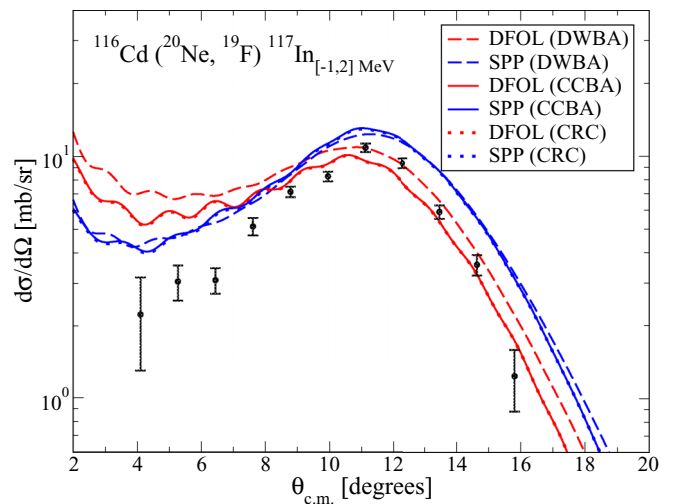


FIG. 4. Experimental angular distribution of the differential cross section for the one-proton transfer reaction $^{116}\text{Cd}(^{20}\text{Ne}, ^{19}\text{F})^{117}\text{In}$, as obtained in the $[-1, 2]$ MeV excitation energy range. Theoretical results refer to three different reaction schemes: DWBA, CCBA, and CRC. Both DFOL and SPP optical potentials are employed.

get a reliable reproduction of the transfer channels. Direct-reaction calculations for the transfer mechanism have been performed by employing EFR transfer coupling within, at first, the DWBA approximation. Following the analysis performed in some recent works [40], it is constructive to also look at the effect of the coupling with the inelastic excitations of low-lying states in the incoming partition within the CCBA or CRC formalism.

To perform microscopic transfer-reaction calculations, one needs to also know the spectroscopic amplitudes associated with the wave-function single-particle overlaps. Such amplitudes are derived through large-scale shell-model calculations performed by using the NUSHELLX code [74].

For projectile-like isotopes, the effective Zuker–Buck–McGrory (z_{bm}) interaction [75] is considered within a model space that assumes ^{12}C as a closed core and valence protons and neutrons in the $1p_{1/2}$, $1d_{5/2}$, and $2s_{1/2}$ orbits. We also checked that similar results would be obtained when employing the $psdmod$ [76] interaction, which was also adopted in some recent works [66,77].

For the target-like isotopes involved here, discrepancies are generally observed in reproducing the single-particle spectrum. Nevertheless, the recently introduced effective interaction $88\text{Sr}45$ [78] allows for a quite satisfying determination of the excitation energy of the low-lying states in this mass region [40]. In that case, ^{88}Sr is assumed as a closed core within a model space which considers valence protons in the $2d_{5/2}$, $2p_{1/2}$, $1g_{9/2}$, and $1g_{7/2}$ orbits and neutrons in the $2d_{5/2}$, $3s_{1/2}$, $1g_{7/2}$, and $2d_{3/2}$ orbits.

The couplings and level schemes obtained considering z_{bm} and $88\text{Sr}45$ interactions for projectile-like and target-like nuclei, respectively, are sketched in Fig. 5, while the spectroscopic amplitudes of the relevant overlaps involved are listed in Table III.

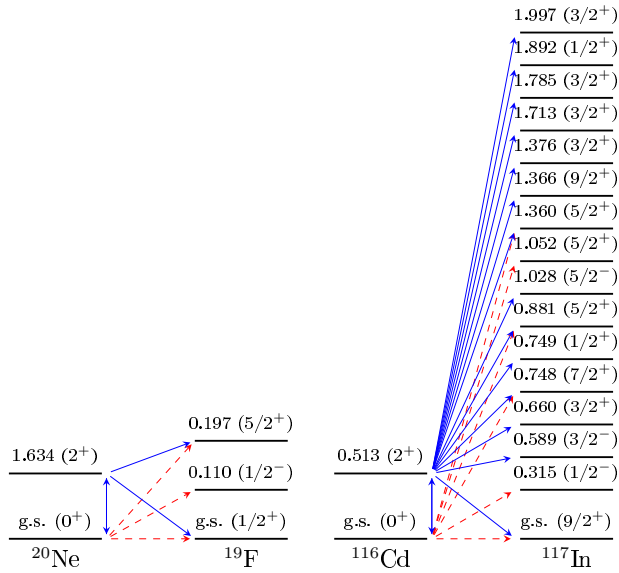


FIG. 5. Coupling schemes of the projectile and target overlaps used in the calculations of the $^{116}\text{Cd}(^{20}\text{Ne}, ^{19}\text{F})^{117}\text{In}$ one-proton transfer reaction, within the considered excitation-energy range. Red dashed arrows concern the coupling considered within the DWBA approximation, while the blue full arrows indicate the additional couplings introduced within the CCBA reaction scheme. In the CRC framework, not shown in the figure, all arrows have to be considered bidirectional (see text).

The single-particle wave functions representing the overlaps are generated by Woods–Saxon binding potentials, whose depths are varied to reproduce the experimental one-proton separation energies. The same procedure is adopted in the following for the one-neutron transfer, where the depths are varied in order to reproduce the experimental one-neutron separation energies. The calculations have been performed by setting the reduced radii and diffuseness parameters of the binding potentials to 1.23 fm and 0.65 fm for $^{116}\text{Cd} + p$ and to 1.26 fm and 0.7 fm for $^{19}\text{F} + p$. Such values are compatible with the systematics usually adopted and allow for the reproduction of the experimental data [40].

The angular distribution of the differential cross section for the $^{116}\text{Cd}(^{20}\text{Ne}, ^{19}\text{F})^{117}\text{In}$ reaction is shown in Fig. 4, as obtained within three different theoretical approaches: DWBA, CCBA, and CRC. In all cases, the postrepresentation is adopted and full complex remnant terms are considered. Moreover, the same prescriptions used in OM calculations are employed to determine the corresponding core-core potential. Both DFOL and SPP optical potentials are employed and the corresponding results are compared with the experimental data discussed above.

Regardless of the reaction framework considered, one may observe that, while the DFOL potential tends to overestimate the contribution at smaller angles, the SPP potential returns a satisfactory agreement of the typical bell shape exhibited by the experimental data around the grazing angle. As shown by the figure, the shape of the angular distribution in the angular range covered by the experimental data depends significantly

TABLE III. One-proton spectroscopic amplitudes (S.A.) adopted in DWBA and CCBA calculation of the $^{116}\text{Cd}(^{20}\text{Ne}, ^{19}\text{F})^{117}\text{In}$ one-proton transfer reaction. These amplitudes are obtained through shell model calculations by employing z_{bm} interaction for projectile-like nuclei and $88S_{r45}$ interaction for target-like ones. The column nl_j indicates the principal quantum number, the orbital and the total angular momentum of the single valence proton, respectively, through the usual spectroscopic notation.

Initial state	Final state	nl_j	S.A.	
$^{20}\text{Ne}_{\text{g.s.}} (0^+)$	$^{19}\text{F}_{\text{g.s.}} (1/2^+)$	($2s_{1/2}$)	-0.8584	
	$^{19}\text{F}_{0.110} (1/2^-)$	($1p_{1/2}$)	-1.2702	
	$^{19}\text{F}_{0.197} (5/2^+)$	($1d_{5/2}$)	1.1741	
$^{20}\text{Ne}_{1.634} (2^+)$	$^{19}\text{F}_{\text{g.s.}} (1/2^+)$	($1d_{5/2}$)	0.6712	
	$^{19}\text{F}_{0.197} (5/2^+)$	($2s_{1/2}$)	-0.6922	
$^{116}\text{Cd}_{\text{g.s.}} (0^+)$	$^{117}\text{In}_{\text{g.s.}} (9/2^+)$	($1g_{9/2}$)	-0.4066	
	$^{117}\text{In}_{0.315} (1/2^-)$	($2p_{1/2}$)	-0.3847	
	$^{117}\text{In}_{0.748} (7/2^+)$	($1g_{7/2}$)	0.0098	
	$^{117}\text{In}_{0.881} (5/2^+)$	($2d_{5/2}$)	-0.1593	
	$^{117}\text{In}_{1.052} (5/2^+)$	($2d_{5/2}$)	-0.2670	
	$^{117}\text{In}_{1.360} (5/2^+)$	($2d_{5/2}$)	-0.7192	
	$^{116}\text{Cd}_{0.513} (2^+)$	$^{117}\text{In}_{\text{g.s.}} (9/2^+)$	($1g_{9/2}$)	-0.6092
			($1g_{7/2}$)	0.0073
			($2d_{5/2}$)	0.1182
		$^{117}\text{In}_{0.589} (3/2^-)$	($2p_{3/2}$)	-0.3319
$^{117}\text{In}_{0.660} (3/2^+)$		($1g_{7/2}$)	-0.0157	
		($2d_{5/2}$)	-0.1502	
$^{117}\text{In}_{0.748} (7/2^+)$		($1g_{9/2}$)	-0.2232	
		($1g_{7/2}$)	0.0170	
		($2d_{5/2}$)	0.0674	
$^{117}\text{In}_{0.749} (1/2^+)$		($2d_{5/2}$)	-0.2796	
$^{116}\text{Cd}_{0.513} (2^+)$	$^{117}\text{In}_{0.881} (5/2^+)$	($1g_{9/2}$)	0.4308	
		($1g_{7/2}$)	0.0201	
		($2d_{5/2}$)	-0.1781	
	$^{117}\text{In}_{1.028} (5/2^-)$	($2p_{1/2}$)	0.3306	
	$^{117}\text{In}_{1.052} (5/2^+)$	($2d_{5/2}$)	0.5693	
		($1g_{9/2}$)	-0.1326	
	$^{117}\text{In}_{1.360} (5/2^+)$	($1g_{9/2}$)	-0.1813	
	$^{117}\text{In}_{1.366} (9/2^+)$	($2d_{5/2}$)	-0.4463	
	$^{117}\text{In}_{1.376} (3/2^+)$	($2d_{5/2}$)	-0.2946	
	$^{117}\text{In}_{1.713} (3/2^+)$	($2d_{5/2}$)	-0.1521	
$^{117}\text{In}_{1.785} (3/2^+)$	($2d_{5/2}$)	0.1214		
$^{117}\text{In}_{1.892} (1/2^+)$	($2d_{5/2}$)	-0.6646		
	($1g_{7/2}$)	0.1382		

on the details of the optical potentials, especially in the surface region. From a qualitative point of view, we verified that the same shape would be preserved, indeed, even when performing the calculations by assuming unitary values for the spectroscopic amplitudes for all the states considered in our coupling scheme of Fig. 5 or when assuming a different effective interaction in our shell-model calculations. So, the result of Fig. 4 confirms the reliability of the potentials adopted to describe the projectile-target interaction, especially for the SPP parametrization. Nevertheless, it provides some hints to distinguish between different options for the optical potentials, which equally well reproduce the experimental

results in the elastic channel, supporting the preferable choice of the SPP potential.

Moreover, not only the shape but also the reproduction of the order of magnitude of the differential cross section is observed in Fig. 4. Such a result, which was reached without the need of any arbitrary scaling factor or any significant modification of the structure parameters of the binding potentials, demonstrates the trustworthiness of the model space and of the effective interaction employed in our shell-model calculations, despite some existing and hard-to-quantify uncertainties.

In Fig. 4, the effect of the coupling with inelastic states in the entrance partition can be inferred from the comparison between the different reaction schemes adopted. Regardless of the optical potential employed, some general features may be discussed. Indeed, similarly to what was observed in our recent work [40], the inclusion of couplings with low-lying collective inelastic excitations moderately changes the shape of the angular distribution. In particular, it slightly modifies the oscillating behavior of the transfer cross section at small angles, owing to the different orbital angular-momentum transferred when passing through the intermediate states involved in the inelastic excitations. Moreover, a tiny shift is introduced on the bell-shaped peak due to the larger spatial distribution of the collective wave functions adopted in the coupled-channel calculations. As would be expected, a larger cross section above the grazing angle is observed in the CCBA compared with the DWBA. Such behavior is attributed to couplings with the target 2_1^+ state, as one observes by selectively switching off the contributions of the various inelastic excitations. As far as the coupling with the projectile 2_1^+ state is concerned, its inclusion does not imply any change in the shape of the differential cross section, except only for a small global reduction, which suggests a destructive interference with the 0^+ state contribution. In Fig. 4, CRC results are also displayed. Whatever the optical potential considered, the curve related to CRC calculation is always practically superimposed on the one corresponding to the CCBA results, in the explored angular region. We recall here that, in CRC calculations, the couplings related to the single-nucleon transfer transitions are implemented iteratively until the absolute difference between successive S -matrix elements becomes less than 0.01%, so even including the back coupling. Therefore, our result demonstrates that accounting for the effect of the latter is safely negligible and this holds not only for the transfer but also for both elastic and inelastic channels. Indeed, in all cases the difference between CRC and CCBA calculations on the total cross section is smaller than 0.2%.

On the other hand, the small differences found between DWBA and CCBA calculations demonstrate a mild influence of the high-order couplings between transfer and scattering channels, at least in the present angular window. The role of the inelastic excitations might be thus disregarded at a first level of accuracy or effectively embedded in the dynamic polarization potential. This is especially true when looking at other quantities, such as the (angular-integrated) total cross section, which is obviously less sensitive to the details of the diffraction pattern.

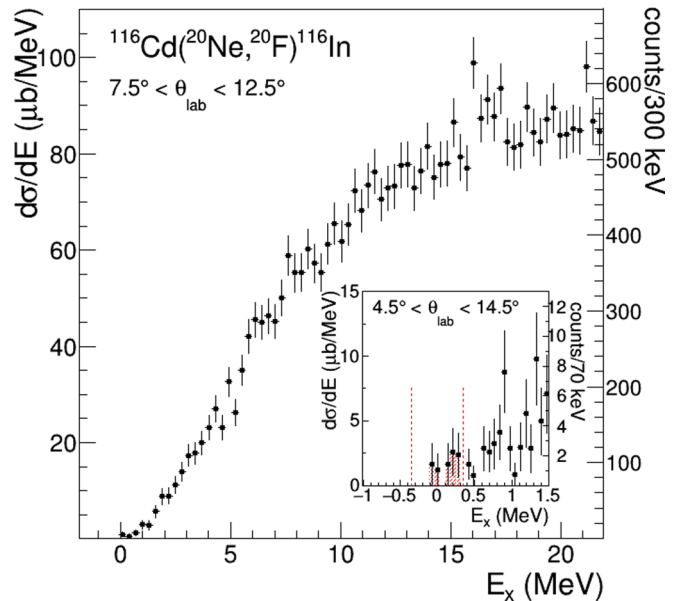


FIG. 6. Excitation-energy cross-section spectrum of the single charge-exchange channel in the $7.5^\circ < \theta_{\text{lab}} < 12.5^\circ$ angular range. In the inset, the spectrum up to 1.5 MeV in the full angular interval $4.5^\circ < \theta_{\text{lab}} < 14.5^\circ$ is reported. The dashed lines and the red hatched area highlight the selected integration energy region discussed in the text.

To summarize, Figs. 2 and 4 show that, with a unified choice of the optical potential and with a rather simple coupling scheme, we are able to reproduce at once the angular distribution of both the quasi-elastic and one-proton transfer channel. Of course, one might in principle consider more sophisticated reaction frameworks or approximations and more complex coupling schemes. Nevertheless, since this simplified approach already demonstrates an acceptable agreement with the experimental data, resorting to more complex reaction schemes is unnecessary, as long as one does not want to describe more channels. Moreover, it allows us to test the basic ingredients of our calculations, validating our choice of the optical potential adopted, as well as the model space and interaction combination considered in the shell-model calculations.

C. Contribution of sequential neutron-proton transfer on the SCE

The (^{20}Ne , ^{20}F) SCE reaction absolute cross-section energy spectrum is shown in Fig. 6. In the inset, a zoom of the excitation energy region up to 1.5 MeV is reported. The continuum shape is a combined effect of the high level density of the involved ejectile and residual nuclei and the limited energy resolution. Such conditions, together with the poor statistics, do not allow for further experimental analysis. Therefore, cross-section values were extracted only by integrating over selected energy ranges, thus including the contributions from transitions to several states of the final partition. To compare the experimental results with the theoretical ones, a small excitation energy interval has been considered, namely, the

TABLE IV. SCE cross section (in μb) as obtained with the SPP and the DFOL potential through two-step transfer mechanisms, when integrating in the angular range $[4.5^\circ, 14.5^\circ]$ of the laboratory system and for all the combination of projectile and target states lying within the considered excitation energy range. The integrated experimental value is also reported.

J_p^π	J_t^π	E_t^*	DFOL		SPP		σ_{expt}
			σ_{DWBA}	σ_{CCBA}	σ_{DWBA}	σ_{CCBA}	
$2_{\text{g.s.}}^+$	1^+	0.000	0.015	0.024	0.020	0.033	
$2_{\text{g.s.}}^+$	5^+	0.128	0.017	0.043	0.019	0.049	
$2_{\text{g.s.}}^+$	4^+	0.223	0.014	0.021	0.018	0.028	
$2_{\text{g.s.}}^+$	2^+	0.273	0.078	0.078	0.099	0.100	
$2_{\text{g.s.}}^+$	4^+	0.313	0.128	0.129	0.153	0.156	
Total			0.252	0.295	0.309	0.366	0.7 ± 0.3

one between -0.35 and 0.35 MeV. The list of the expected states in the selected energy interval for the ejectile and the residual nuclei and the corresponding experimental integrated cross section are listed in Table IV.

In the present work, we focus on the competing multinucleon transfer mechanisms which end up in the same exit channel as the one reached in the direct SCE process. Hence, in our approach, all excited states in either the projectile- or the target-like outgoing nuclei is thus populated only through the proper rearrangement of neutrons and protons.

A schematic representation of the two different paths considered is sketched in Fig. 7: the same final states may then be reached by performing either a one-neutron pickup followed by a one-proton stripping (hereafter labeled as path 1) or viceversa (hereafter labeled as path 2).

In the following, the two different reaction paths will be first considered separately and thereafter will be included within the same scheme in order to evaluate the interference between the two processes. The prior-post-representation is used and full complex remnant terms are considered.

Before embarking on the full calculations, we also checked the equivalence between the different (prior-post) representations adopted, once the nonorthogonality terms are included [79]. We compare thus the prior-post-calculation for which nonorthogonality terms identically vanish [42], with two other

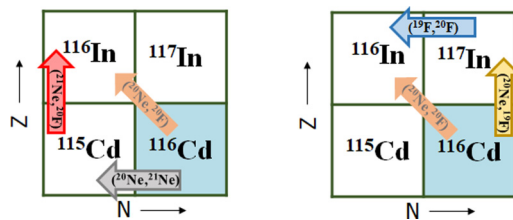


FIG. 7. Schematic representation of the sequential neutron-proton transfer processes, discussed before in Sec. II. The one-neutron pickup + one-proton stripping [path 1, Eq. (2)] and the one-proton stripping + one-neutron pickup [path 2, Eq. (3)] routes are depicted on the left and right, respectively. For completeness, the direct SCE channel is also indicated.

possible combinations, where nonorthogonality corrections are included. As a result, a very nice agreement is generally observed. Such an agreement, even though is never worse than 3%, slightly deteriorates for larger angles (beyond 15°), where, however, the differential cross section has a steep decrease and its contribution to the total integrated value practically vanishes. Such a result confirms in turn the good numerical convergence of our calculations. In the second transfer steps of path 1 and path 2, contributions of spectroscopic strength less than 0.1 are neglected.

a. Path 1. Let us consider path 1, whose couplings and level schemes of the involved nuclei are sketched in Fig. 8. The values of the spectroscopic amplitudes extracted by the shell-model calculation, when employing *zbm* and *88Sr45* interaction, are listed in Table V for projectile-like overlaps and in Tables VI and VII for target-like overlaps involved in the first and in the second transfer steps, respectively.

As one may observe in Fig. 8, there is a large number of states in the intermediate partition which may be coupled, especially when target-like excitation levels are considered. Moreover, the coupling between two different states may involve even more overlaps, as indicated in Tables VI and VII. In principle, one should consider in fact all the possible states of the intermediate partition and, therefore, extend as much as possible the number of couplings included. However, at least when taking into account transitions which involve low-lying states of projectile and target in the initial partition as in this case, the coupling with states having larger excitation energy should be generally reduced.

Moreover, in view of the comparison with the experimental data, which may isolate the contribution to the low-lying states also of the final partition, a further reduction of the weight of high-energy contributions to the total cross section is expected. Nevertheless, these states may play a role within CCBA formalism, whereas the coupling with the 2_1^+ states of the initial partition is explicitly taken into account. However, in that case, their contribution is expected to be suppressed by the larger number of steps involved in the whole process. In any case, complete CCBA calculations have been also performed to get a quantitative estimation of these contributions.

b. Path 2. Analogously to the analysis of the previous paragraph, a two-step transfer reaction calculation through the intermediate partition ($^{19}\text{F} + ^{117}\text{In}$) has been performed, at first within the DWBA approximation. Couplings and level schemes of the involved nuclei are sketched in Fig. 9. The values of the spectroscopic amplitudes extracted by the shell-model calculation, when employing *zbm* and *88Sr45* interactions, for projectile-like and target-like overlaps, are listed in Tables VIII and IX, respectively.

c. Coherent sum of two paths. With the aim to properly evaluate the role of the two-step transfer mechanisms in determining the total cross section of the $^{116}\text{Cd}(^{20}\text{Ne}, ^{20}\text{F})^{116}\text{In}$ SCE reaction, the contribution of the two different paths illustrated above should be included in a coherent way within the same calculation. The resulting angular behavior of the differential angular distribution cross section, as obtained within the DWBA approximation along path 1 or path 2 or when including the coherent sum of the two paths, is shown in Fig. 10

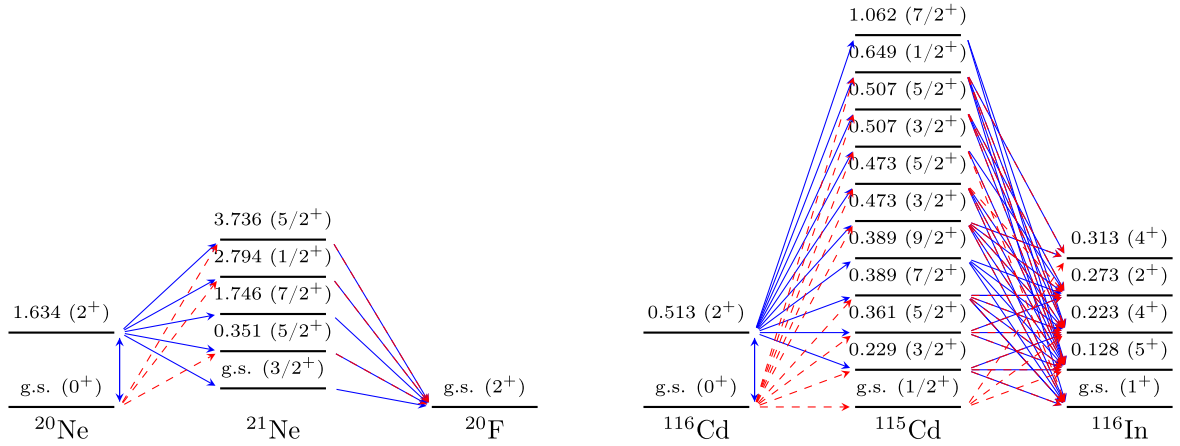


FIG. 8. Coupling schemes of the projectile and target overlaps used in the sequential two-nucleon transfer reaction calculations, along path 1. The z_{bm} and $88S_{r45}$ interactions are employed in shell-model calculations, for projectile-like and target-like nuclei, respectively. Red arrows concern the coupling considered within the DWBA approximation, while the blue arrows indicate the additional couplings introduced within the CCBA reaction scheme.

for the different target-like states lying within the excitation energy range considered. For the projectile-like states, only the g.s. is taken into account. Only the SPP parametrization is, moreover, shown for the optical potential, for sake of simplicity.

As a general feature, one observes that the bell shape exhibited by the angular distribution in the one-proton transfer case

TABLE V. Spectroscopic amplitudes (S.A.) obtained through shell-model z_{bm} interaction and adopted in CCBA calculations for all the projectile-like nuclei involved along the path 1 (see text) of the $^{116}\text{Cd}(^{20}\text{Ne}, ^{20}\text{F})^{116}\text{In}$ SCE reaction, whose final states lie within the excitation energy range here considered. The column nl_j indicates the principal quantum number, the orbital and the total angular momentum of the single valence proton, respectively, through the usual spectroscopic notation.

Initial state	Final state	nl_j	S.A.
$^{20}\text{Ne}_{\text{g.s.}} (0^+)$	$^{21}\text{Ne}_{0.351} (5/2^+)$	$(1d_{5/2})$	0.7696
	$^{21}\text{Ne}_{2.794} (1/2^+)$	$(2s_{1/2})$	-0.7355
	$^{21}\text{Ne}_{3.736} (5/2^+)$	$(1d_{5/2})$	-0.0891
	$^{21}\text{Ne}_{\text{g.s.}} (3/2^+)$	$(2s_{1/2})$	0.2077
$^{20}\text{Ne}_{1.634} (2^+)$	$^{21}\text{Ne}_{\text{g.s.}} (3/2^+)$	$(1d_{5/2})$	-1.0262
	$^{21}\text{Ne}_{0.351} (5/2^+)$	$(2s_{1/2})$	0.3181
		$(1d_{5/2})$	0.1650
	$^{21}\text{Ne}_{1.746} (7/2^+)$	$(1d_{5/2})$	-0.9131
	$^{21}\text{Ne}_{2.794} (1/2^+)$	$(1d_{5/2})$	-0.6516
	$^{21}\text{Ne}_{3.736} (5/2^+)$	$(2s_{1/2})$	-0.7344
		$(1d_{5/2})$	0.5534
$^{21}\text{Ne}_{\text{g.s.}} (3/2^+)$	$^{20}\text{F}_{\text{g.s.}} (2^+)$	$(2s_{1/2})$	-0.6366
		$(1d_{5/2})$	0.5209
$^{21}\text{Ne}_{0.351} (5/2^+)$		$(2s_{1/2})$	0.0656
		$(1d_{5/2})$	-0.6412
		$(1d_{5/2})$	-0.4159
$^{21}\text{Ne}_{1.746} (7/2^+)$		$(1d_{5/2})$	-0.4159
$^{21}\text{Ne}_{2.794} (1/2^+)$		$(1d_{5/2})$	-0.0431
$^{21}\text{Ne}_{3.736} (5/2^+)$		$(2s_{1/2})$	-0.0331
		$(1d_{5/2})$	-0.2296

is modified in the sequential two-step transfer mechanism. The result is, up to a large extent, a quite flat angular behavior of the differential cross section, at least at intermediate angles. Moreover, for a given combination of states in the exit channel, the diffraction pattern seems to be practically independent from the considered path while it depends on the angular momentum of the final states involved, i.e., on the total angular-momentum transferred in the process. In particular, at least from a qualitative point of view, one notices that the angular position of the first maximum shifts to larger angles when considering target states in the outgoing partition with larger J values. However, this correspondence, which is easily recovered in the one-nucleon transfer case, is blended and less clear in the two-step process where an intermediate partition is crossed. As a consequence, some differences arise in the diffraction pattern at small angles even when the angular momentum of the target states in the final partition is the same (see, for example, the differences existing in the diffraction patterns for the two different 4^+ states of ^{116}In shown in Fig. 10).

A remarkable feature to be noted is that the contribution provided along path 1 is systematically larger than the corresponding one obtained along path 2. Such a result might be mainly attributed to the larger level density predicted in the low-excitation-energy region for the system ^{115}Cd , with respect to the ^{117}In , within the model space here adopted.

In addition, the role of the coherent interference between the two path turns out to be rather important. The coherent sum of the two contributions may considerably alter indeed the diffraction pattern of the general process, especially when the two paths have a comparable magnitude. As a result, the angular distribution of the differential cross section might appear rather different from the single-path components, whereas the absolute cross section is only partially affected.

Similar conclusions might be drawn when more complicated coupling schemes are investigated. For this purpose, it could be helpful to compare the DWBA results with the CCBA ones in order to shed light on the role of the inelastic

TABLE VI. Spectroscopic amplitudes (S.A.) obtained through shell-model 88Sr45 interaction and adopted in CCBA calculations for all the target-like nuclei involved along the first step of path 1 (see text) of the $^{116}\text{Cd}(^{20}\text{Ne}, ^{20}\text{F})^{116}\text{In}$ SCE reaction. The column nl_j indicates the principal quantum number, the orbital and the total angular momentum of the single valence proton, respectively, through the usual spectroscopic notation.

Initial state	Final state	nl_j	S.A.
$^{116}\text{Cd}_{g.s.} (0^+)$	$^{115}\text{Cd}_{g.s.} (1/2^+)$	$(3s_{1/2})$	0.8913
	$^{115}\text{Cd}_{0.229} (3/2^+)$	$(2d_{3/2})$	-1.2814
	$^{115}\text{Cd}_{0.361} (5/2^+)$	$(2d_{5/2})$	-0.0927
	$^{115}\text{Cd}_{0.389} (7/2^+)$	$(1g_{7/2})$	1.8526
	$^{115}\text{Cd}_{0.473} (3/2^+)$	$(2d_{3/2})$	0.0356
	$^{115}\text{Cd}_{0.473} (5/2^+)$	$(2d_{5/2})$	0.3192
	$^{115}\text{Cd}_{0.507} (3/2^+)$	$(2d_{3/2})$	-0.0219
	$^{115}\text{Cd}_{0.507} (5/2^+)$	$(2d_{5/2})$	0.0950
	$^{115}\text{Cd}_{0.649} (1/2^+)$	$(3s_{1/2})$	0.9347
	$^{116}\text{Cd}_{0.513} (2^+)$	$^{115}\text{Cd}_{0.229} (3/2^+)$	$(3s_{1/2})$
		$(2d_{3/2})$	0.9889
		$(1g_{7/2})$	-0.1855
$^{115}\text{Cd}_{0.361} (5/2^+)$		$(3s_{1/2})$	-0.5688
		$(2d_{3/2})$	0.5895
		$(1g_{7/2})$	0.3823
$^{115}\text{Cd}_{0.389} (7/2^+)$		$(2d_{1/2})$	-0.1917
		$(1g_{3/2})$	0.5723
$^{115}\text{Cd}_{0.389} (9/2^+)$		$(2d_{5/2})$	0.1209
		$(1g_{3/2})$	-0.5996
$^{115}\text{Cd}_{0.473} (3/2^+)$		$(3s_{1/2})$	-0.4137
		$(1g_{7/2})$	-0.2472
$^{115}\text{Cd}_{0.473} (5/2^+)$		$(3s_{1/2})$	0.1866
		$(1g_{7/2})$	0.5306
$^{115}\text{Cd}_{0.507} (3/2^+)$		$(3s_{1/2})$	0.1228
		$(2d_{5/2})$	0.1089
		$(1g_{7/2})$	-0.4713
$^{115}\text{Cd}_{0.507} (5/2^+)$		$(3s_{1/2})$	-0.1367
		$(2d_{3/2})$	0.2446
		$(1g_{7/2})$	-0.2707
$^{115}\text{Cd}_{0.649} (1/2^+)$	$(2d_{3/2})$	-0.2863	
	$(2d_{5/2})$	0.1247	
$^{115}\text{Cd}_{1.062} (7/2^+)$	$(2d_{3/2})$	0.5040	
	$(1g_{7/2})$	0.4286	

excitations and on the transfer mechanisms which they are involved in. The corresponding results are displayed in Fig. 11, where the differential cross section is plotted as a function of the scattering angle in the center-of-mass system. Only the total cross section, given by the coherent sum of the two path contributions and the incoherent sum on combinations of projectile and target states lying within the excitation energy range considered is reported. As in the one-nucleon transfer case, the CCBA results only slightly impact the diffraction pattern at forward angles, in light of the different combinations of states and of angular-momentum transfer involved when exploring the intermediate partition. The results are then slightly sensitive also to the choice of the optical potential in view of the delicate interplay between the spatial

TABLE VII. Spectroscopic amplitudes (S.A.) obtained through shell-model 88Sr45 interaction and adopted in CCBA calculations for all the target-like nuclei involved along the second step of path 1 (see text) of the $^{116}\text{Cd}(^{20}\text{Ne}, ^{20}\text{F})^{116}\text{In}$ SCE reaction and whose final states lie within the excitation energy range here considered. The column nl_j indicates the principal quantum number, the orbital and the total angular momentum of the single valence proton, respectively, through the usual spectroscopic notation.

Initial state	Final state	nl_j	S.A.		
$^{115}\text{Cd}_{0.229} (3/2^+)$	$^{116}\text{In}_{g.s.} (1^+)$	$(2d_{5/2})$	-0.1978		
		$(1g_{9/2})$	-0.9798		
		$(1g_{9/2})$	0.3486		
		$(2d_{5/2})$	-0.1457		
		$(2d_{5/2})$	0.1498		
		$(2d_{5/2})$	-0.1540		
		$(2d_{5/2})$	0.1505		
		$(1g_{9/2})$	0.2514		
		$^{115}\text{Cd}_{g.s.} (1/2^+)$	$^{116}\text{In}_{0.128} (5^+)$	$(1g_{9/2})$	-0.3145
				$(1g_{9/2})$	0.5385
$(1g_{9/2})$	0.1772				
$(1g_{9/2})$	-0.2004				
$(2d_{5/2})$	-0.1084				
$(1g_{9/2})$	-0.2877				
$(1g_{9/2})$	-0.2605				
$(1g_{9/2})$	0.1585				
$(1g_{9/2})$	-0.2633				
$(1g_{9/2})$	0.1831				
$^{115}\text{Cd}_{0.229} (3/2^+)$	$^{116}\text{In}_{0.223} (4^+)$	$(1g_{9/2})$	-0.4179		
		$(1g_{9/2})$	-0.4774		
		$(2d_{5/2})$	-0.1412		
		$(1g_{9/2})$	0.5945		
		$(1g_{9/2})$	0.1464		
		$(2d_{5/2})$	0.1171		
		$(1g_{9/2})$	-0.8536		
		$(1g_{9/2})$	0.1176		
		$(1g_{9/2})$	-0.4535		
		$(1g_{9/2})$	-0.2989		
$^{115}\text{Cd}_{0.361} (5/2^+)$	$^{116}\text{In}_{0.273} (2^+)$	$(1g_{9/2})$	0.2337		
		$(1g_{9/2})$	0.5216		
		$(2d_{5/2})$	-0.1858		
		$(2d_{5/2})$	-0.1401		
		$(1g_{9/2})$	0.5919		
		$(1g_{9/2})$	-0.4539		
		$(2d_{5/2})$	0.1242		
		$(1g_{9/2})$	-0.1142		
		$(2d_{5/2})$	0.1230		
		$(2d_{5/2})$	-0.1611		
$^{115}\text{Cd}_{g.s.} (1/2^+)$	$^{116}\text{In}_{0.313} (4^+)$	$(1g_{9/2})$	-0.1678		
		$(1g_{9/2})$	0.1308		
		$(1g_{9/2})$	-0.3518		

extension of the transition form factor and the surface details of the ion-ion interaction. Indeed, analogously to what was observed also in Fig. 4 for the one-proton-transfer case, DFOL results tend to be larger at small angles but predict

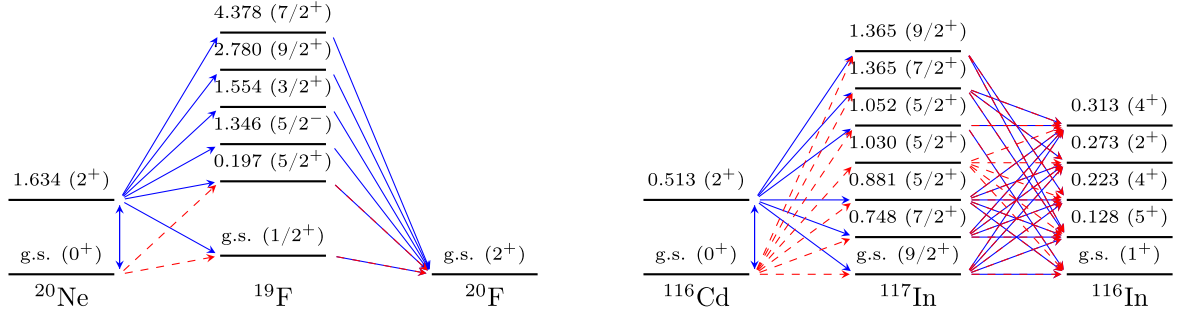


FIG. 9. Coupling schemes of the projectile and target overlaps used in the sequential two-nucleon transfer reaction calculations, along path 2. The z_{bm} and $88Sr45$ interactions are employed in shell-model calculations for projectile-like and target-like nuclei, respectively. Red arrows concern the coupling considered within the DWBA approximation, while the blue arrows indicate the additional couplings introduced within the CCBA reaction scheme.

a steeper decrease than SPP with increasing $\theta_{c.m.}$ scattering angle.

The results discussed above allow us thus to finally achieve a quantitative estimation of the total SCE cross section, at least when describing this process as only given by the sequence of two-nucleon transfer mechanisms and inelastic excitations in the initial partition. Although the genuine direct SCE transition driven by the direct isovector nuclear interaction is not included in such a scheme, it is thus certainly worthwhile to provide a first comparison with the experimental results. In Table IV, we list the theoretical cross section, integrated in the angular range $[4.5^\circ, 14.5^\circ]$ of the laboratory system, for all the states lying within the considered excitation energy range. In

TABLE VIII. Spectroscopic amplitudes (S.A.) obtained through shell-model z_{bm} interaction and adopted in CCBA calculations for all the projectile-like nuclei involved along the path 2 (see text) of the $^{116}\text{Cd}(^{20}\text{Ne}, ^{20}\text{F})^{116}\text{In}$ SCE reaction and whose final states lie within the excitation energy range here considered. The column nl_j indicates the principal quantum number, the orbital and the total angular momentum of the single valence proton, respectively, through the usual spectroscopic notation.

Initial state	Final state	nl_j	S.A.
$^{20}\text{Ne}_{g.s.} (0^+)$	$^{19}\text{F}_{g.s.} (1/2^+)$	$(2s_{1/2})$	-0.8584
	$^{19}\text{F}_{0.197} (5/2^+)$	$(1d_{5/2})$	1.1741
$^{20}\text{Ne}_{1.634} (2^+)$	$^{19}\text{F}_{g.s.} (1/2^+)$	$(1d_{5/2})$	0.6712
	$^{19}\text{F}_{0.197} (5/2^+)$	$(2s_{1/2})$	-0.6922
		$(1d_{5/2})$	-0.6416
	$^{19}\text{F}_{1.346} (5/2^-)$	$(1p_{1/2})$	-0.9779
	$^{19}\text{F}_{1.554} (3/2^+)$	$(2s_{1/2})$	0.3767
		$(1d_{5/2})$	0.2923
$^{19}\text{F}_{g.s.} (1/2^+)$	$^{19}\text{F}_{2.780} (9/2^+)$	$(1d_{5/2})$	-0.6248
	$^{19}\text{F}_{4.378} (7/2^+)$	$(1d_{5/2})$	-0.1995
	$^{20}\text{F}_{g.s.} (2^+)$	$(1d_{5/2})$	-0.2291
$^{19}\text{F}_{0.197} (5/2^+)$		$(2s_{1/2})$	0.1215
		$(1d_{5/2})$	-0.8891
$^{19}\text{F}_{1.346} (5/2^-)$		$(1p_{1/2})$	-0.1475
$^{19}\text{F}_{1.554} (3/2^+)$		$(1d_{5/2})$	-0.4445
$^{19}\text{F}_{2.780} (9/2^+)$		$(1d_{5/2})$	-0.5137
$^{19}\text{F}_{4.378} (7/2^+)$		$(1d_{5/2})$	-0.5312

Table IV, we also reported the total sum, to be compared with the corresponding experimental value.

In light of the results of Table IV, one can assess that, when describing the $^{116}\text{Cd}(^{20}\text{Ne}, ^{20}\text{F})^{116}\text{In}$ reaction only in terms of two successive transfer processes, the order of magnitude of the cross section is nicely recovered in our theoretical calculations. Moreover, this is achieved already within the simplified DWBA framework, although the role of the coupling with the inelastic excitations of the states which belong to the initial partition seems to be not completely negligible.

It is also worth noting that, due to the finite experimental energy resolution, the set interval upper limit rules out part of the high-energy contributions of the considered transitions. On the other hand, the present theoretical predictions of the sequential proton-neutron transfer processes fully account for such contributions, leading to an expected overestimation of the relative amount in the total reaction cross section attributed to the multistep mechanism. Nonetheless, this does not affect the validity of this first study, since the order of magnitude of the transfer processes would be in any case preserved.

We would like to recall here that our result has been obtained by employing as theoretical ingredients an optical potential, which has demonstrated to provide a reliable reproduction of the elastic channel, and a well-defined model space with its corresponding shell-model effective interaction, which returns a satisfying spectroscopic description of the nuclear systems involved here and allows for reasonable agreement with experimental results of the one-proton transfer process. We notice, by the way, that the same ingredients have already been successfully applied in the description of two-neutron and two-proton transfer reactions, having in common the same initial partition [40].

Of course, our result might still be considered affected by a certain degree of model dependence, as suggested by the small sensitivity here highlighted with respect to the optical potential adopted and to the fine details of the structure ingredients. This unavoidable model dependence, which might be ascribable to the variety of different processes involved and to the uncertainties existing in the description of the considered nuclei, is, however, strongly mitigated in our work by the multichannel experimental constraints and the fully consistent theoretical approach employed. Moreover, our study suggests that SPP might be globally considered a preferable choice

TABLE IX. Spectroscopic amplitudes (S.A.) obtained through shell-model $88\text{Sr}45$ interaction and adopted in CCBA calculations for all the target-like nuclei involved along the path 2 (see text) of the $^{116}\text{Cd}(^{20}\text{Ne}, ^{20}\text{F})^{116}\text{In}$ SCE reaction and whose final states lie within the excitation energy range here considered. The column nl_j indicates the principal quantum number, the orbital and the total angular momentum of the single valence proton, respectively, through the usual spectroscopic notation.

Initial state	Final state	nl_j	S.A.
$^{116}\text{Cd}_{g.s.} (0^+)$	$^{117}\text{In}_{g.s.} (9/2^+)$	$(1g_{7/2})$	-0.4066
	$^{117}\text{In}_{0.748} (7/2^+)$	$(1g_{7/2})$	0.0098
	$^{117}\text{In}_{0.881} (5/2^+)$	$(2d_{5/2})$	-0.1593
	$^{117}\text{In}_{1.030} (5/2^+)$	$(2d_{5/2})$	-0.2670
	$^{117}\text{In}_{1.052} (5/2^+)$	$(2d_{5/2})$	-0.7192
	$^{117}\text{In}_{1.365} (7/2^+)$	$(1g_{7/2})$	-0.0027
	$^{117}\text{In}_{1.365} (9/2^+)$	$(1g_{9/2})$	0.0383
$^{116}\text{Cd}_{0.513} (2^+)$	$^{117}\text{In}_{g.s.} (9/2^+)$	$(2d_{5/2})$	0.1182
		$(1g_{9/2})$	-0.6092
	$^{117}\text{In}_{0.748} (7/2^+)$	$(1g_{9/2})$	-0.2232
	$^{117}\text{In}_{0.881} (5/2^+)$	$(2d_{5/2})$	-0.1781
		$(1g_{9/2})$	0.4308
	$^{117}\text{In}_{1.052} (5/2^+)$	$(2d_{5/2})$	0.5693
		$(1g_{9/2})$	-0.1326
	$^{117}\text{In}_{1.365} (7/2^+)$	$(2d_{5/2})$	0.1889
	$^{117}\text{In}_{1.365} (9/2^+)$	$(1g_{9/2})$	-0.1813
$^{117}\text{In}_{g.s.} (9/2^+)$	$^{116}\text{In}_{g.s.} (1^+)$	$(1g_{7/2})$	-0.5008
$^{117}\text{In}_{0.881} (5/2^+)$		$(2d_{3/2})$	-0.2335
$^{117}\text{In}_{1.030} (5/2^+)$		$(2d_{3/2})$	-0.4548
$^{117}\text{In}_{1.052} (5/2^+)$		$(2d_{3/2})$	0.2233
$^{117}\text{In}_{g.s.} (9/2^+)$	$^{116}\text{In}_{0.128} (5^+)$	$(1g_{7/2})$	-0.1534
		$(2d_{3/2})$	-0.9107
		$(3s_{1/2})$	-0.1969
$^{117}\text{In}_{0.748} (7/2^+)$		$(1g_{7/2})$	0.1283
		$(2d_{3/2})$	0.7751
$^{117}\text{In}_{0.881} (5/2^+)$		$(2d_{5/2})$	0.1249
$^{117}\text{In}_{1.030} (5/2^+)$		$(1g_{7/2})$	0.1178
$^{117}\text{In}_{1.365} (7/2^+)$		$(2d_{3/2})$	-0.4105
$^{117}\text{In}_{1.365} (9/2^+)$		$(1g_{7/2})$	-0.1519
		$(2d_{3/2})$	-0.4675
$^{117}\text{In}_{g.s.} (9/2^+)$	$^{116}\text{In}_{0.223} (4^+)$	$(2d_{3/2})$	0.6852
		$(3s_{1/2})$	-0.2581
		$(1g_{7/2})$	0.1143
$^{117}\text{In}_{0.748} (7/2^+)$		$(2d_{3/2})$	0.2821
$^{117}\text{In}_{0.881} (5/2^+)$		$(2d_{3/2})$	0.9649
$^{117}\text{In}_{1.030} (5/2^+)$		$(2d_{3/2})$	-0.4573
$^{117}\text{In}_{1.365} (9/2^+)$		$(3s_{1/2})$	-0.1604
$^{117}\text{In}_{g.s.} (9/2^+)$	$^{116}\text{In}_{0.273} (2^+)$	$(1g_{7/2})$	0.6212
		$(2d_{3/2})$	-0.1605
		$(2d_{3/2})$	0.1612
		$(2d_{3/2})$	0.3029
		$(2d_{3/2})$	-0.3473
		$(2d_{3/2})$	-0.1060
		$(2d_{3/2})$	-0.2653
	$(3s_{1/2})$	-0.8248	
$^{117}\text{In}_{0.748} (7/2^+)$		$(2d_{3/2})$	-0.1569
$^{117}\text{In}_{0.881} (5/2^+)$		$(2d_{3/2})$	0.1433
$^{117}\text{In}_{1.030} (5/2^+)$		$(2d_{3/2})$	0.2034
$^{117}\text{In}_{1.052} (5/2^+)$		$(2d_{3/2})$	-0.1049
$^{117}\text{In}_{1.365} (7/2^+)$		$(2d_{3/2})$	0.2134

with respect to DFOL. Although they both give a good reproduction of the scattering data, SPP gives indeed a better description of the transfer channels, in one-proton transfer as well as in the two-neutron and two-proton channels considered in Ref. [40].

The analysis performed here thus does not prevent us from drawing important conclusions. On the one hand, our work demonstrates that the two-step transfer mechanisms provide a non-negligible contribution to the total cross section of the $^{116}\text{Cd}(^{20}\text{Ne}, ^{20}\text{F})^{116}\text{In}$ reaction channel. Such a result, in the energy or mass range investigated in the present work, was not so obvious. Although in some previous works (Refs. [32–35]), which mainly refer to lighter systems, a primary role of the multistep transfer contribution was already assessed, in some other light-ion-induced studies (Ref. [30]), a different behavior was observed, thus highlighting a nonuniversal scenario. Moreover, in this work, different kinematical conditions, which are of crucial importance in determining the magnitude of the transfer mechanisms, have been generally explored. On the other hand, our finding suggests that a relevant fraction of this total cross section is still missing within our picture. Such a fraction should be provided by the direct mechanism, namely, from the direct SCE process, which has not been addressed here, owing to unavoidable uncertainties which would affect the results for a such a heavy system, both from the experimental and theoretical perspectives. Such a statement might then be definitely validated only when confirmed by a consistent calculation taking into account the direct charge-exchange contribution. Nevertheless, for the time being, we highlight that this result seems to be in line with recent findings discussed in Ref. [23], where a significant contribution from a direct isovector exchange mechanism is highlighted from the analysis of the $^{40}\text{Ca}(^{18}\text{O}, ^{18}\text{F})^{40}\text{K}$ SCE reaction at the same bombarding energy per nucleon.

The competition between the two processes is, however, anything but trivial, since its fully consistent analysis would require all the structure ingredients needed for describing both mechanisms being extracted within the same coherent theoretical framework. Such a competition is currently under investigation and will be the topic of a forthcoming presentation.

However, since the transfer mechanisms do not seem to be suppressed, the present study already suggests that, in order to extract structure information on the NME from the SCE cross section, a careful estimation of the competing transfer processes is needed. These higher-order processes are instead expected to be suppressed when further increasing the number of steps involved, for example, when investigating DCE reactions, and preliminary attempts along this direction seem to confirm such an expectation [31,40].

V. CONCLUSIONS AND OUTLOOKS

In the present work, the $^{116}\text{Cd}(^{20}\text{Ne}, ^{20}\text{F})^{116}\text{In}$ reaction has been studied at an incident energy of 306 MeV through a multichannel analysis involving also the elastic scattering and the one-proton-transfer $^{116}\text{Cd}(^{20}\text{Ne}, ^{19}\text{F})^{117}\text{In}$ reaction. Such

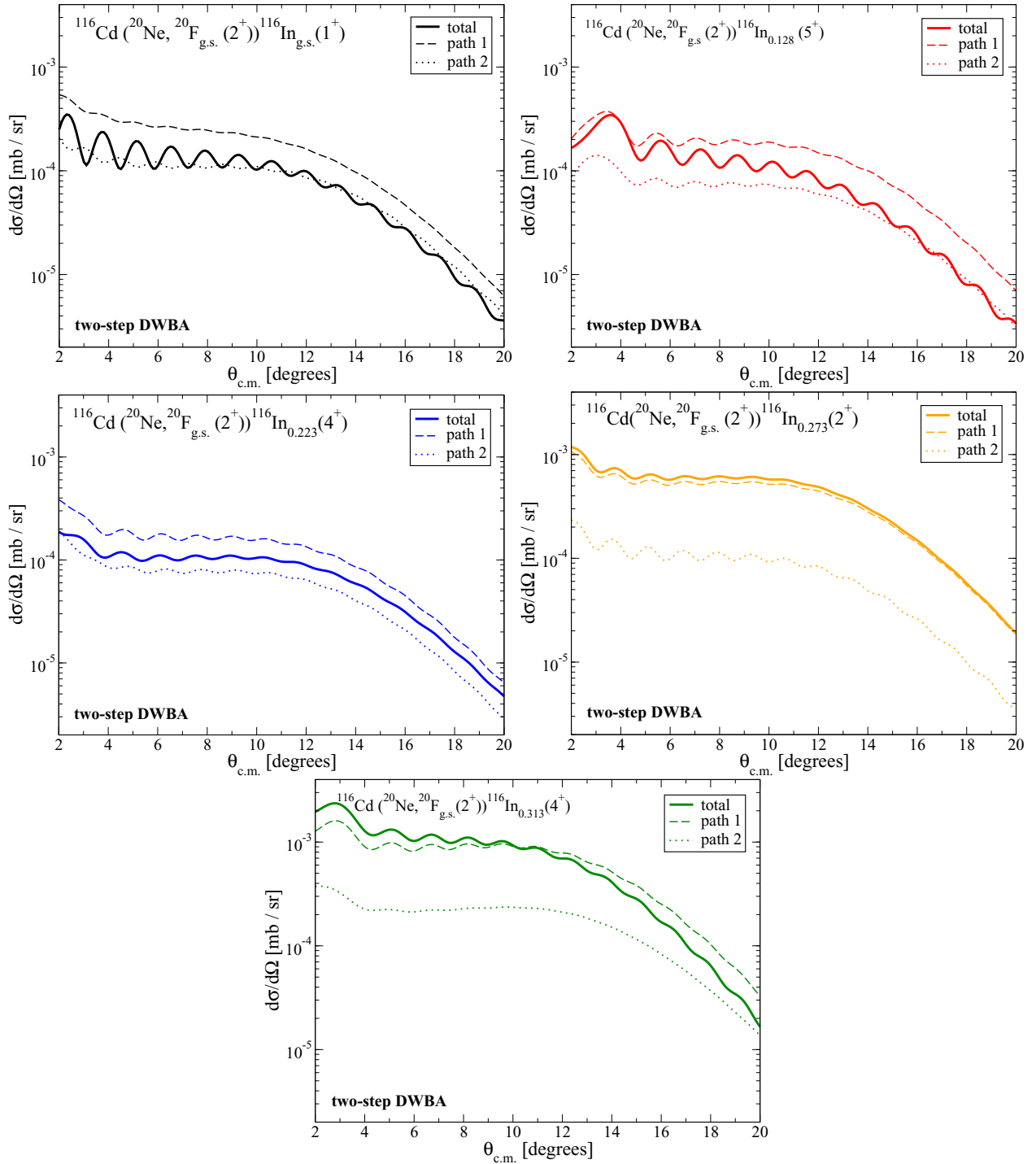


FIG. 10. Angular distribution of the differential cross section for the different final states of the $^{116}\text{Cd}(^{20}\text{Ne}, ^{20}\text{F}_{\text{g.s.}}(2^+))^{116}\text{In}$ SCE reaction, lying within the considered excitation energy range, as obtained when considering only the two-step transfer mechanisms. The two-step DWBA approximation is adopted and the SPP optical potential is employed. The two paths are considered separately and with their coherent sum.

a wide collection of experimental data was indeed instrumental to put more stringent constraints on the nuclear models that are also adopted for the calculations of the SCE direct process, the corresponding NME, and the related beta-decay ones. In perspective, studying CE reactions on ^{116}Cd will contribute to

encircle and to understand the expected $0\nu 2\beta$ -decay properties of that nucleus.

The experimental data for multinucleon transfer have been then compared with the theoretical predictions obtained by performing (sequential) two-step distorted-wave Born

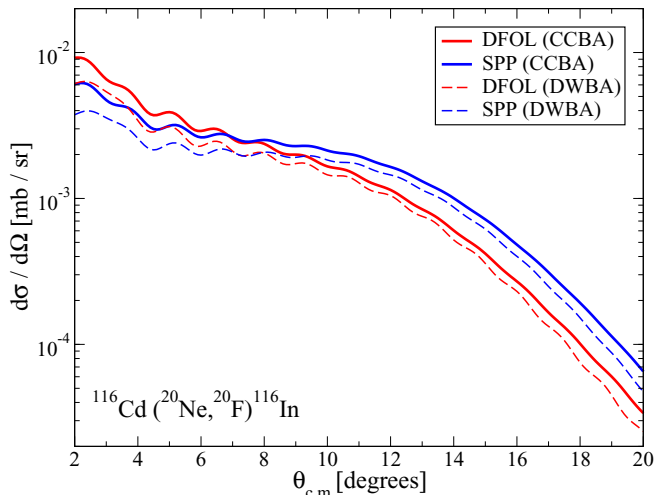


FIG. 11. Angular distribution of the differential cross section for all the final states of the $^{116}\text{Cd}(^{20}\text{Ne}, ^{20}\text{F})^{116}\text{In}$ SCE reaction lying within the considered excitation energy range and obtained from the two-step DWBA (dashed lines) or CCBA (full lines) calculations. Calculation with the DFOL and SPP ion-ion potentials are indicated by red and blue lines, respectively.

approximation and higher-order coupled reaction channel calculations. Two different optical potentials were employed for modeling the initial- and final-state interactions, and a large-scale shell-model approach was adopted to evaluate the spectroscopic amplitudes for the single-particle transitions characterizing one-nucleon transfer processes.

Through a combination of structure and reaction studies and a multichannel comparison with the experimental data, we validated the choice of the optical potentials adopted and we checked the reliability of the model space and interactions assumed in the shell-model calculations. Moreover, we shed light on the influence of the high-order couplings between transfer and scattering channels, bringing to light a bland influence of the inelastic excitations in the initial partition both on the one-proton transfer process and on the SCE reaction.

Finally, within the same unified scheme, our calculations were able to reproduce also the order of magnitude of the experimental cross section by describing the $^{116}\text{Cd}(^{20}\text{Ne}, ^{20}\text{F})^{116}\text{In}$ reaction only in terms of successive transfer processes. This result was obtained already within the simplified two-step DWBA framework, proving that resorting to more complex reaction schemes, at a first level of accuracy, is unnecessary. It is worth noting that the robustness of our finding is corroborated by the fact that no parameter has been practically adjusted with respect to the systematics.

However, the sequence of second- or higher-order transfer or inelastic processes considered in our study does not entirely exhaust the total cross section. The origin of the remaining difference between the theoretical and experimental results is not easy to access at this stage, although being for a large extent ascribable to the direct SCE mechanism, which is not included within the present picture. Our conclusion is thus that room is left for a possible contribution of the direct isovector exchange mechanism in the explored SCE transitions.

The genuine contribution of the latter mechanism might be isolated when a fully consistent analysis, taking into account the competition among all the possible processes involved, including the direct SCE mechanism, is carried out within the same theoretical framework. As a perspective, the study of the competition among the different charge-exchange reaction mechanisms demands the exploration of new set of data. To this aim, the analysis of simple systems, in which transitions to individual states can be isolated, is particularly helpful for untangling direct and multistep contributions and comparing with the predictions of theoretical models. Studies of heavy-ion-induced charge-exchange transitions on ^{12}C target are already in progress [80], taking advantage of the low level density in the light reaction products and of the well-known spectroscopic properties of the involved nuclei. In this view, the analysis of new charge-exchange data at different beam energies is also interesting and it is among the research lines of the NUMEN and NURE projects [12]. Work is in progress along this direction, with the aim of extending this analysis also to the DCE channel, which is of particular interest for the possibility to extract information on the NME of 2β decay.

ACKNOWLEDGMENTS

The authors warmly acknowledge the operators of INFN-LNS Accelerator Division for the production and delivery of the ^{20}Ne beam and their support throughout the experiments. This project has received funding from the European Research Council (ERC) under the European Union's Horizon 2020 Research and Innovation Program (Grant Agreement No. 714625). S.B. and J.A.L. acknowledge support from the Spanish Ministry of Economy and Competitiveness and the European Regional Development Fund (FEDER) under Projects No. FIS2017-88410-P and No. FIS2014-53448-C2-1-P. E.R.C.-L. acknowledges DGAPA-UNAM IN107820, AG101120 and CONACyT 314857. J.R.B.O. acknowledges "FAPESP proc. 2019/07767-1 and INCT-FNA, Project No. 464898/2014-5, Brazil, by JRBO," DGAPA-UNAM IN107820, AG101120 and CONACyT 314857.

- [1] F. Osterfeld, *Rev. Mod. Phys.* **64**, 491 (1992).
- [2] M. Ichimura, H. Sakai, and T. Wakasa, *Prog. Part. Nucl. Phys.* **56**, 446 (2006).
- [3] D. Frekers *et al.*, *Nucl. Phys. A* **916**, 219 (2013).
- [4] C. Brendel *et al.*, *Nucl. Phys. A* **477**, 162 (1988).

- [5] B. D. Anderson, N. Tamimi, A. R. Baldwin, M. Elaasar, R. Madey, D. M. Manley, M. Mostajaboddavati, J. W. Watson, W. M. Zhang, and C. C. Foster, *Phys. Rev. C* **43**, 50 (1991).
- [6] J. Blomgren *et al.*, *Phys. Lett. B* **362**, 34 (1995).
- [7] K. Yako *et al.*, *Phys. Lett. B* **615**, 193 (2005).

- [8] D. Frekers, *Prog. Part. Nucl. Phys.* **57**, 217 (2006).
- [9] H. Fujita, Y. Fujita, T. Adachi, A. D. Bacher, G. P. A. Berg, T. Black, E. Caurier, C. C. Foster, H. Fujimura, K. Hara, K. Harada, K. Hatanaka, J. Janecke, J. Kamiya, Y. Kanzaki, K. Katori, T. Kawabata, K. Langanke, G. Martínez-Pinedo, T. Noro, D. A. Roberts, H. Sakaguchi, Y. Shimbara, T. Shinada, E. J. Stephenson, H. Ueno, T. Yamanaka, M. Yoshifuku, and M. Yosoi, *Phys. Rev. C* **75**, 034310 (2007).
- [10] Y. Fujita, B. Rubio, and W. Gelletly, *Prog. Part. Nucl. Phys.* **66**, 549 (2011).
- [11] C. A. Douma *et al.*, *Eur. Phys. J. A* **56**, 51 (2020).
- [12] F. Cappuzzello *et al.*, *Eur. Phys. J. A* **54**, 72 (2018).
- [13] F. Cappuzzello *et al.*, *Eur. Phys. J. A* **51**, 145 (2015).
- [14] C. Agodi *et al.*, *Nucl. Part. Phys. Proc.* **265-266**, 28 (2015).
- [15] C. Agodi *et al.*, *Universe* **7**, 72 (2021).
- [16] M. Sasano, H. Sakai, K. Yako, T. Wakasa, M. Dozono, V. Rodin, A. Faessler, K. Fujita, M. B. Greenfield, K. Hatanaka, K. Itoh, T. Kawabata, H. Kuboki, Y. Maeda, K. Miki, K. Muto, S. Noji, H. Okamura, Y. Sakemi, K. Sekiguchi, Y. Shimizu, Y. Sasamoto, Y. Tameshige, A. Tamii, and T. Uesaka, *Phys. Rev. C* **85**, 061301(R) (2012).
- [17] K. Kisamori *et al.*, *Phys. Rev. Lett.* **116**, 052501 (2016).
- [18] K. Miki *et al.*, *Phys. Lett. B* **769**, 339 (2017).
- [19] T. N. Taddeucci *et al.*, *Nucl. Phys. A* **469**, 125 (1987).
- [20] W. P. Alford and B. M. Spicer, *Adv. Nucl. Phys.* **24**, 1 (1998).
- [21] H. Lenske *et al.*, *Prog. Part. Nucl. Phys.* **109**, 103716 (2019).
- [22] H. Lenske, J. I. Bellone, M. Colonna, and J. A. Lay, *Phys. Rev. C* **98**, 044620 (2018).
- [23] M. Cavallaro *et al.*, *Front. Astron. Space Sci.* **8**, 659815 (2021).
- [24] J. I. Bellone *et al.*, *Phys. Lett. B* **807**, 135528 (2020).
- [25] Lenske *et al.*, *Universe* **7**, 98 (2021).
- [26] E. Santopinto, H. Garcia-Tecocoatzi, R. I. Magaña Vsevolodovna, J. Ferretti *et al.* (NUMEN Collaboration), *Phys. Rev. C* **98**, 061601(R) (2018).
- [27] J. Engel and J. Menéndez, *Rep. Prog. Phys.* **80**, 046301 (2017).
- [28] N. Shimizu, J. Menéndez, and K. Yako, *Phys. Rev. Lett.* **120**, 142502 (2018).
- [29] D. Gambacurta, M. Grasso, and J. Engel, *Phys. Rev. Lett.* **125**, 212501 (2020).
- [30] F. Cappuzzello *et al.*, *Nucl. Phys. A* **739**, 30 (2004).
- [31] J. A. Lay *et al.*, *J. Phys.: Conf. Ser.* **1056**, 012029 (2018).
- [32] W. von Oertzen, *Nucl. Phys. A* **482**, 357 (1988).
- [33] J. S. Winfield, N. Anantaraman, S. M. Austin, L. H. Harwood, J. van der Plicht, H. L. Wu, and A. F. Zeller, *Phys. Rev. C* **33**, 1333 (1986); **35**, 1166(E) (1987).
- [34] H. Lenske, H. H. Wolter, and H. G. Bohlen, *Phys. Rev. Lett.* **62**, 1457 (1989).
- [35] C. H. Dasso and A. Vitturi, *Phys. Rev. C* **34**, 743 (1986).
- [36] A. Spatafora, F. Cappuzzello, D. Carbone, M. Cavallaro, J. A. Lay, L. Acosta, C. Agodi, D. Bonanno, D. Bongiovanni, I. Boztosun, G. A. Brischetto, S. Burrello, S. Calabrese, D. Calvo, E. R. Chavez Lomeli, I. Ciraldo, M. Colonna, F. Delaunay, N. Deshmukh, J. L. Ferreira, P. Finocchiaro, M. Fisichella, A. Foti, G. Gallo, A. Hacısalihoglu, F. Iazzi, G. Lanzalone, H. Lenske, R. Linares, D. LoPresti, J. Lubian, M. Moralles, A. Muoio, J. R. B. Oliveira, A. Pakou, L. Pandola, H. Petrascu, F. Pinna, S. Reito, G. Russo, G. Santagati, O. Sgouros, S. O. Solakci, V. Soukeras, G. Souliotis, D. Torresi, S. Tudisco, A. Yildirim, and V. A. B. Zagatto, *Phys. Rev. C* **100**, 034620 (2019).
- [37] L. La Faiuci *et al.*, *Phys. Rev. C* **104**, 054610 (2021).
- [38] O. Sgouros, M. Cavallaro, F. Cappuzzello, D. Carbone, C. Agodi, A. Gargano, G. DeGregorio, C. Altana, G. A. Brischetto, S. Burrello, S. Calabrese, D. Calvo, V. Capirossi, E. R. Chavez Lomeli, I. Ciraldo, M. Cutuli, F. Delaunay, H. Djapo, C. Eke, P. Finocchiaro, M. Fisichella, A. Foti, A. Hacısalihoglu, F. Iazzi, L. La Faiuci, R. Linares, J. Lubian, N. H. Medina, M. Moralles, J. R. B. Oliveira, A. Pakou, L. Pandola, F. Pinna, G. Russo, M. A. Guazzelli, V. Soukeras, G. Souliotis, A. Spatafora, D. Torresi, A. Yildirim, and V. A. B. Zagatto, *Phys. Rev. C* **104**, 034617 (2021).
- [39] D. Carbone *et al.*, *Universe* **7**, 58 (2021).
- [40] D. Carbone, J. L. Ferreira, S. Calabrese, F. Cappuzzello, M. Cavallaro, A. Hacısalihoglu, H. Lenske, J. Lubian, R. I. Magnana Vsevolodovna, E. Santopinto, C. Agodi, L. Acosta, D. Bonanno, T. Borello-Lewin, I. Boztosun, G. A. Brischetto, S. Burrello, D. Calvo, E. R. Chavez Lomeli, I. Ciraldo, M. Colonna, F. Delaunay, N. Deshmukh, P. Finocchiaro, M. Fisichella, A. Foti, G. Gallo, F. Iazzi, L. La Faiuci, G. Lanzalone, R. Linares, N. H. Medina, M. Moralles, J. R. B. Oliveira, A. Pakou, L. Pandola, H. Petrascu, F. Pinna, S. Reito, G. Russo, O. Sgouros, S. O. Solakci, V. Soukeras, G. Souliotis, A. Spatafora, D. Torresi, S. Tudisco, A. Yildirim, and V. A. B. Zagatto, *Phys. Rev. C* **102**, 044606 (2020).
- [41] J. L. Ferreira, D. Carbone, M. Cavallaro, N. N. Deshmukh, C. Agodi, G. A. Brischetto, S. Calabrese, F. Cappuzzello, E. N. Cardozo, I. Ciraldo, M. Cutuli, M. Fisichella, A. Foti, L. La Faiuci, O. Sgouros, V. Soukeras, A. Spatafora, D. Torresi, and J. Lubian (NUMEN Collaboration), *Phys. Rev. C* **103**, 054604 (2021).
- [42] G. R. Satchler, *Direct Nuclear Reactions* (Oxford University Press, Oxford and New York, 1983).
- [43] N. K. Timofeyuk and R. C. Jonhson, *Prog. Part. Nucl. Phys.* **111**, 103738 (2020).
- [44] D. Montanari, S. Leoni, L. Corradi, G. Pollarolo, G. Benzoni, N. Blasi, S. Bottoni, A. Bracco, F. Camera, A. Corsi, F. C. L. Crespi, B. Million, R. Nicolini, O. Wieland, G. de Angelis, F. Della Vedova, E. Fioretto, A. Gadea, B. Guiot, D. Mengoni, D. R. Napoli, R. Orlandi, F. Recchia, A. M. Stefanini, R. P. Singh, J. J. Valiente-Dobon, D. Bazzacco, E. Farnea, S. M. Lenzi, S. Lunardi, G. Montagnoli, F. Scarlassara, C. Ur, G. Lo Bianco, A. Zucchiatti, S. Szilner, M. Kmiecik, A. Maj, and W. Meczynski, *Phys. Rev. C* **84**, 054613 (2011).
- [45] L. R. Gasques, A. S. Freitas, L. C. Chamon, J. R. B. Oliveira, N. H. Medina, V. Scarduelli, E. S. Rossi, M. A. G. Alvarez, V. A. B. Zagatto, J. Lubian, G. P. A. Nobre, I. Padron, and B. V. Carlson, *Phys. Rev. C* **97**, 034629 (2018).
- [46] T. Tamura, *Phys. Rep.* **14**, 59 (1974).
- [47] N. Keeley, K. W. Kemper, and K. Rusek, *Phys. Rev. C* **102**, 014617 (2020).
- [48] I. J. Thompson, *Comput. Phys. Rep.* **7**, 167 (1988).
- [49] M. Cavallaro *et al.*, *Nucl. Instrum. Methods Phys. Res., Sect. B* **463**, 334 (2020).
- [50] K. Shima, N. Kuno, M. Yamanouchi, and H. Tawara, *At. Data Nucl. Data Tables* **51**, 173 (1992).
- [51] M. Cavallaro *et al.*, *Results Phys.* **13**, 102191 (2019).
- [52] F. Cappuzzello, C. Agodi, D. Carbone, and M. Cavallaro, *Eur. Phys. J. A* **52**, 167 (2016).

- [53] F. Cappuzzello *et al.*, *Nucl. Instrum. Methods Phys. Res., Sect. A* **621**, 419 (2010).
- [54] M. Cavallaro *et al.*, *Eur. Phys. J. A* **48**, 59 (2012).
- [55] D. Torresi *et al.*, *Nucl. Instrum. Methods Phys. Res., Sect. A* **989**, 164918 (2021).
- [56] D. Pereira *et al.*, *Phys. Lett. B* **670**, 330 (2009).
- [57] D. Pereira *et al.*, *Phys. Lett. B* **710**, 426 (2012).
- [58] L. M. Fonseca, R. Linares, V. A. B. Zagatto, F. Cappuzzello, D. Carbone, M. Cavallaro, C. Agodi, J. Lubian, and J. R. B. Oliveira, *Phys. Rev. C* **100**, 014604 (2019).
- [59] D. Pereira *et al.*, *Nucl. Phys. A* **826**, 211 (2009).
- [60] V. A. B. Zagatto, F. Cappuzzello, J. Lubian, M. Cavallaro, R. Linares, D. Carbone, C. Agodi, A. Foti, S. Tudisco, J. S. Wang, J. R. B. Oliveira, and M. S. Hussein, *Phys. Rev. C* **97**, 054608 (2018).
- [61] M. A. G. Alvarez *et al.*, *Nucl. Phys. A* **723**, 93 (2003).
- [62] M. A. Franey and W. G. Love, *Phys. Rev. C* **31**, 488 (1985).
- [63] B. Pritychenko, M. Birch, B. Singh, and M. Horoi, *At. Data Nucl. Data Tables* **107**, 1 (2016).
- [64] S. Raman and C. W. Nestor, and P. Tikkanen, *At. Data Nucl. Data Tables* **78**, 1 (2001).
- [65] G. R. Satchler and W. G. Love., *Phys. Rep.* **55**, 183 (1979).
- [66] D. Carbone, J. L. Ferreira, F. Cappuzzello, J. Lubian, C. Agodi, M. Cavallaro, A. Foti, A. Gargano, S. M. Lenzi, R. Linares, and G. Santagati, *Phys. Rev. C* **95**, 034603 (2017).
- [67] B. Paes, G. Santagati, R. M. Vsevolodovna, F. Cappuzzello, D. Carbone, E. N. Cardozo, M. Cavallaro, H. Garcia-Tecocoatzi, A. Gargano, J. L. Ferreira, S. M. Lenzi, R. Linares, E. Santopinto, A. Vitturi, and J. Lubian, *Phys. Rev. C* **96**, 044612 (2017).
- [68] M. J. Ermamatov, R. Linares, J. Lubian, J. L. Ferreira, F. Cappuzzello, D. Carbone, M. Cavallaro, M. Cubero, P. N. de Faria, A. Foti, G. Santagati, and V. A. B. Zagatto, *Phys. Rev. C* **96**, 044603 (2017).
- [69] M. J. Ermamatov, F. Cappuzzello, J. Lubian, M. Cubero, C. Agodi, D. Carbone, M. Cavallaro, J. L. Ferreira, A. Foti, V. N. Garcia, A. Gargano, J. A. Lay, S. M. Lenzi, R. Linares, G. Santagati, and A. Vitturi, *Phys. Rev. C* **94**, 024610 (2016).
- [70] B. Pritychenko, M. Birch, B. Singh, and M. Horoi, *At. Data Nucl. Data Tables* **114**, 371 (2017).
- [71] T. Kibedi and R. H. Spear, *At. Data Nucl. Data Tables* **80**, 35 (2002).
- [72] D. M. Brink, *Phys. Lett. B* **40**, 37 (1972).
- [73] S. Kahana and A. J. Baltz, *Adv. Nucl. Phys.* **9**, 1 (1977).
- [74] W. D. M. Rae, <http://www.garsington.eclipse.co.uk>.
- [75] A. P. Zuker, B. Buck, and J. B. McGrory, *Phys. Rev. Lett.* **21**, 39 (1968).
- [76] Y. Utsuno and S. Chiba, *Phys. Rev. C* **83**, 021301(R) (2011).
- [77] E. N. Cardozo, J. Lubian, R. Linares, F. Cappuzzello, D. Carbone, M. Cavallaro, J. L. Ferreira, A. Gargano, B. Paes, and G. Santagati, *Phys. Rev. C* **97**, 064611 (2018).
- [78] L. Coraggio, A. Gargano, and N. Itaco, *Phys. Rev. C* **93**, 064328 (2016).
- [79] I. J. Thompson, in *Fifty Years of Nuclear BCS, Pairing in Finite Systems*, edited by R. A. Broglia and V. Zelevinsky (World Scientific, 2013), pp. 455–467.
- [80] A. Spatafora *et al.* (unpublished).